Word Count: 12963 Revision 3

Quartz textures, trace elements, fluid inclusions, and in-situ oxygen isotopes from Aktogai porphyry Cu deposit, Kazakhstan

Changhao Li [1,3], Ping Shen [1,2,3*], Reimar Seltmann [4], Di Zhang [5,2], Hongdi Pan [6], Eleonora Seitmuratova [7]

[1]Key Laboratory of Mineral Resources, Institute of Geology and Geophysics, Chinese Academy of Sciences, Beijing 100029, China;

[2]University of Chinese Academy of Sciences, Beijing 100049, China;

[3]Institutions of Earth Science, Chinese Academy of Sciences, Beijing 100029, China;

[4]Center for Russian and Central EurAsian Mineral Studies, Natural History Museum, London SW7 5BD, UK

[5]State Key Laboratory of Lithospheric Evolution, Institute of Geology and Geophysics, Chinese Academy of Sciences, Beijing 100029, China

[6]College of Earth Sciences, Chang'an University, Xi'an 710054, China

[7]Laboratory of Geological Formations, K. Satpaev Institute of Geological Sciences, Almaty 050010, Kazakhstan

Corresponding author:

Name: Ping Shen

E-mail: pshen@mail.iggcas.ac.cn

Abstract

The Paleozoic Aktogai Group in Kazakhstan ranks among the thirty largest porphyry Cu deposits globally. The Aktogai deposit is the largest one in the Aktogai Group and is characterized by intensive potassic alteration where the dominant orebody occurred. However, its mineralization processes remain unclear. Our investigation focused on the texture, trace elements, fluid inclusions, and in-situ oxygen isotopes of the quartz from the ore-related tonalite porphyry and associated potassic alteration at Aktogai to trace the deposit's mineralization processes. Ti-in-quartz thermobarometry, fluid inclusion microthermometry, and geological characteristics indicate that the ore-related magma at Aktogai originated from a shallow magma chamber at ~1.9±0.5 kbar (~7.2±1.9 km) and intruded as the tonalite porphyry stock at ~1.7-2.4 km. The potassic alteration and associated Cu mineralization comprise five types of veins (A1, A2, B1, B2, and C) and two types of altered rocks (biotite and K-feldspar). Among them, nine types of hydrothermal quartz were identified from early to late: (1) VQ_{A1} in A1 veins and RQ_{bt} in biotite altered rocks, (2) VQ_{A2} in A2 veins and RQ_{kfs} in K-feldspar altered rocks, (3) VQ_{B1} in B1 veins and VQ_{B2E} in B2 veins, and (4) quartz associated with Cu-Fe sulfides (VQ_{B2L}, VQ_{BC}, and VQ_{C}) in B and C veins. Titanium contents of the quartz decreased, while Al/Ti ratios increased from early to late. Fluid inclusion microthermometry and mineral thermometers reveal that VQ_{A1}, RQ_{bt}, and hydrothermal biotite formed under high-temperature (~470-560 °C) and ductile conditions. VQ_{A2}, RQ_{kfs}, VQ_{B1}, and hydrothermal K-feldspar formed during the transition stage from ductile to brittle, with temperatures of ~350-540 °C. The rapid decrease in pressure from lithostatic to hydrostatic pressure led to fluid boiling and minor involvement of meteoric water (~11-14 %) in the mineralizing fluid. Extensive recrystallization in VQ_{A1} to VQ_{B1} was associated with repeated cleavage and healing of the intrusion. With cooling, K-feldspar decomposition and hydrolysis increased. Fluid cooling and water-rock reactions resulted in the co-precipitation of Cu-Fe sulfides, white mica, chlorite, VQ_{BC}, and VQ_{C}, with temperatures of ~275-370 °C and brittle conditions. The Paleozoic Aktogai deposit exhibits formation depths and fluid evolution processes similar to Mesozoic and Cenozoic PCDs worldwide. The close association between Cu-Fe sulfides and later quartz formed under intermediate-temperature conditions at Aktogai implies that Cu-Fe sulfides are not precipitated during early high-temperature conditions in porphyry Cu deposits.

Keywords: Fluid evolution, Emplacement depth, Fluid source, Ti-in-quartz thermobarometry, Central Asian Orogenic Belt

Introduction

Porphyry Cu deposits (PCDs) are associated with shallow-emplaced intrusions (<5 km) and provide enormous Cu (~75 %), Mo (~50 %), and Au (~20 %) resources to the global supply (Sillitoe 2010). While extensive research has been conducted on the mineralization process of Mesozoic and Cenozoic PCDs (e.g., Seedorff et al. 2005;

Richards 2011; Hou et al. 2015; Yang et al. 2016), studies focusing on Paleozoic PCDs are relatively limited. The Central Asian Orogenic Belt (CAOB) hosts most of the world's Paleozoic PCDs, such as Oyu Tolgoi in Mongolia, Kalmakyr-Dalnee in Uzbekistan, and Aktogai Group in Kazakhstan. Previous studies on Paleozoic PCDs in the CAOB have predominantly examined the tectonic setting, mineralization ages, natures of ore-related magma, and factors influencing PCD size (Zvezdov et al. 1993; Müller et al. 2010; Yakubchuk et al. 2012; Shen et al. 2013, 2015, 2018; Chen et al. 2014; Seltmann et al. 2014; Cao et al. 2016; Porter 2016; Li et al. 2019a). Only a few giant Cu deposits (>3.162 Mt; Cooke et al., 2005) have been extensively studied in terms of mineralization processes, such as Tuwu-Yandong (Shen et al. 2014a, b; Wang et al. 2019, 2021). This limitation hinders the comprehensive understanding of mineralization processes for Paleozoic PCDs in the CAOB and their comparison with Mesozoic and Cenozoic PCDs worldwide.

The Aktogai Group, situated in the North Balkhash metallogenic belt of the western part of the CAOB (Seltmann and Porter 2005), ranks among the thirty largest PCDs globally and is the 3rd largest in the CAOB, containing 11.5 Mt of Cu, 84 t of Au, and 0.3 Mt of Mo. It encompasses the Aktogai, Aidarly, and Kyzilkia deposits, with Aktogai being the largest. Previous studies have discussed the fluid properties of the Aktogai deposit using fluid inclusions and hydrothermal minerals (Zvezdov et al. 1993; Seltmann et al. 2014; Li et al. 2018a, b). However, the absence of scanning electron microscope-cathodoluminescence (SEM-CL) and in-situ quartz oxygen isotopes has limited the investigation of the mineralization process at Aktogai. Moreover, the physicochemical conditions of ore-related magma at Aktogai remain unclear.

In this study, CL images, Ti and Al compositions, fluid inclusions, and in-situ oxygen isotopes of various types of quartz from the ore-related tonalite porphyry and associated potassic alteration at Aktogai are used to examine the physicochemical conditions of ore-related magma, mineralizing fluids, and their evolution.

Regional and deposit geology

Regional geology

The CAOB is one of the world's largest accretionary orogenic belts and records a tectonic evolutionary history spanning ~800 Myr from ~1000 Ma and ~200 Ma (Windley et al. 2007). The intricate Paleozoic cycles of tectonic and magmatic accretion have established the CAOB as a renowned Cu, Au, and Mo metallogenic province (Fig. 1a).

The North Balkhash metallogenic belt contains two giant PCDs (i.e., Aktogai Group and Kounrad deposits). Strata within this belt consist of three units: Precambrian metamorphic basements, Paleozoic folded sedimentary and volcanic rocks, and Mesozoic to Cenozoic sandstone and mudstone (Fig. 1b; Heinhorst et al. 2000). Intrusions in this belt are mainly intermediate-acid rocks, originating from Proterozoic to Permian eras, with a concentrated occurrence during the Late Paleozoic period. Popov (1996) classified intrusions into four types, namely pre-, early-, syn-, and post-orogenic intrusions. Therein, Cu±Au±Mo and Au deposits are associated with pre- and early-orogenic intermediate-acid intrusions, Mo and W deposits with syn-orogenic granites and leucogranite, and Mo±W±Be±Bi polymetallic deposits with post-orogenic leucogranite (Heinhorst et al. 2000).

Deposit geology

The Aktogai deposit is situated at the northeast terminus of Lake Balkhash. As per the Mining Data Solutions database (https://miningdataonline.com/property/4616/Aktogay-Mine.aspx), the Aktogai deposit has 1915 Mt of mineral resources (measured and indicated) with a Cu grade of 0.33 % (~6.3 Mt Cu) and 0.008 % Mo by-product (~0.2 Mt Mo). At Aktogai, volcanic sedimentary strata and intrusions are widely exposed. The strata include the Middle and Upper Carboniferous Keregetasskaya Formation, characterized by andesites interspersed with minor rhyolites, sandstones, and siltstones, as well as the Upper Carboniferous-Lower Permian Koldarskaya Formation, comprising sedimentary rocks, volcanic sedimentary rocks, and minor acidic tuffs (Fig. 2a). The Koldar Complex, intruding into the Keregetasskaya Formation, is composed of gabbro-diorite to granite, with quartz diorite and granodiorite prevailing (Fig. 2a). The Koldar Complex forms at ~366 to ~336 Ma (Li et al. 2012; Chen et al. 2014; Cao et al. 2016) and exhibits geochemical characteristics of low Sr/Y and $(La/Yb)_N$ (N represents the C1 chondrite normalization) ratios, alongside elevated Y and Yb contents, indicative of formation through partial melting of the normal lower crust (Shen et al. 2013; Cao et al. 2016). The ore-related tonalite porphyry intruded into the granodiorite of the Koldar Complex (Fig. 2b). Tonalite porphyry forms at ~331.4 to ~327.5 Ma (Li et al. 2012; Chen et al. 2014;

Cao et al. 2016; Shen et al. 2018) and displays geochemical signatures marked by high Sr/Y and $(La/Yb)_N$ ratios, coupled with low Y and Yb contents, suggesting formation through partial melting of the thickened lower crust (>40 km) (Cao et al. 2016; Shen et al. 2018).

Three types of alterations and associated veins are recognized in the Aktogai deposit: potassic, propylitic, and phyllic alterations (Fig. 2c).

The potassic alteration occurred in the periphery of the barren quartz core and is the main alteration that controls the annular orebody. Hydrothermal minerals associated with this alteration were dominated by K-feldspar and quartz, followed by biotite and Fe-Ti oxides. K-feldspar is observed as fine-grained replacements after plagioclase or within the groundmass (Fig. 3a), occasionally coexisting with fine-grained quartz. Biotite and Fe-Ti oxides occurred locally, predominantly replacing mafic minerals. Five types of veins (A1, A2, B1, B2, and C; Fig. 4) were identified using the classification established by Gustafson and Hunt (1975) and Gustafson and Quiroga (1995). The earliest veins (called A1 veins; <300 μm at width; Fig. 3b) were quartz veinlets and stockwork with discontinuous and obscure walls (Fig. 3b), entirely composed of sugar-granular quartz. A2 veins, which contain quartz with K-feldspar but lack sulfide, mainly comprise K-feldspar-dominated (quartz-free) and quartz-K-feldspar (quartz-rich) veins (Figs. 3b, c, 4), intersecting A1 veins. Quartz grains in A2 veins typically grow perpendicular to the walls. B and C veins are characterized by sulfide mineralization. B1 veins display continuous and relatively planar walls (Fig. 3d, e) and are distinguished by larger quartz grains (up to 3 mm) compared to A veins. Hydrothermal minerals, primarily including K-feldspar, chalcopyrite, molybdenite, pyrite, and white mica, are mainly distributed within B1 veins, with minor molybdenite and K-feldspar also precipitating along the vein margins (Fig. 4). B2 veins are characterized by continuous and planar walls, with a linear distribution of sulfides along the center (Fig. 3f). B2 veins contain large quartz grains and thin K-feldspar halos, with chalcopyrite, pyrite, and chlorite as the predominant hydrothermal minerals. C veins, which truncate A and B veins, are sulfide-chlorite-bearing veins (Fig. 3d, e). They are dominated by sulfide and silicate, with significant variations in quartz volume observed at different locations (Fig. 4). The transition from A1 to C veins is marked by a progression towards regular and planar vein walls, accompanied by an increase in the euhedral degrees and size of quartz grains. Copper and Mo mineralization at Aktogai primarily consists of chalcopyrite, molybdenite, and bornite, occurring both within veins and disseminated throughout the rocks. The potassic alteration underwent a superposition of phyllic and propylitic alterations, resulting in the transformation of K-feldspar to white mica and biotite to chlorite.

The periphery of the Aktogai deposit is surrounded by a large propylitic halo (Fig. 2c), which comprises both deep and shallow propylitic alterations (Li et al. 2018b). The deep propylitic alteration zone is adjacent to the potassic alteration, with hydrothermal K-feldspar present in altered rocks. Hydrothermal minerals in this zone include chlorite, epidote, prehnite, pyrite, and chalcopyrite. Sulfides are either disseminated within altered rocks or precipitated in pyrite-dominated (called D veins) and C veins. In contrast, the shallow propylitic alteration zone, lacking metal mineralization, is far from the potassic alteration and is characterized by the development of chlorite and calcite without hydrothermal K-feldspar.

The phyllic alteration exhibits a discontinuous linear zone, predominantly occurring within the fractured area at the contact between the tonalite porphyry and orebody (Fig. 2c). Throughout this zone, white mica and chlorite are ubiquitous and show compositional variations. Li et al. (2018a) found that, with decreasing temperature, the MgO content of chlorite increases while the FeO content decreases; additionally, the composition of white mica shifts from being governed by $Fe^{2+}+Si^{4+}\rightarrow 2Al^{3+}$ substitution to being controlled by $Fe^{3+}\rightarrow Al^{3+}$ substitution. Sulfides, occurring as dissemination, include chalcopyrite, pyrite, molybdenite, and bornite. Phyllic alteration is accompanied by minor C and D veins. This alteration overlays the potassic alteration, contributing to the formation of the high-grade orebody.

Samples and methods

All samples were selected from the surface and open pit of the Aktogai deposit (Fig. 2a). Detailed information for the analyzed samples is presented in ESM Table 1. All measurements were performed at the Institute of Geology and Geophysics, Chinese Academy of Sciences (IGGCAS).

CL images of quartz were obtained using a MonoCL4 electron microprobe with 15 kV accelerating voltage before trace element analysis. Trace elements of quartz were analyzed using a CAMECA SXFive electron microprobe with a voltage of 15 kV, a beam current of 300 nA, a spot size of 5 μm, and a 240 s peak counting time. The calibration standards were natural albite (Al) and synthetic TiO_2 (Ti). Standardization for calibration standard was performed with a beam current of 20 nA and with a peak counting time of 20 s. Quartz standards developed by Audétat et al. (2014) were used as the secondary reference standard. To avoid the secondary fluorescence effect on measurements, analyzed spots distance at least 50 μm (mostly >100 μm) from minerals and/or inclusions with high Ti and/or Al contents. The detection limits were determined with the Cameca software using background statistics and the 3-sigma criterion as recommended by Ancey et al. (1978). The averages of detection limits and uncertainties for Ti are ~12 ppm and ~10 ppm, and for Al are ~11 ppm and ~10 ppm, respectively. Some data contaminated with white mica were discarded (ESM Fig. 1). Summary and detailed Ti and Al contents of different types of quartz are shown in Table 1 and ESM Tables 2 and 3, respectively. Three Ti-in-quartz thermobarometers, namely Thomas et al. (2010), Huang and Audétat (2012), and Zhang et al. (2020), were used to estimate the formation pressure of magmatic quartz (i.e., P_{T10}, P_{H12}, and P_{Z20}) and the formation temperature of hydrothermal quartz (i.e., T_{T10}, T_{H12}, and T_{Z20}) in this study.

Gas and mineral compositions of individual fluid inclusions were analyzed using a Renishaw1000 Raman microspectrometer following the method of Burke (2001). After finding the fluid inclusion being tested by microscopic observation, the laser beam with a wavelength of 514.5 nm and a spot size of 1 μm was focused on the bubble or daughter mineral. Microthermometry studies of fluid inclusions were carried out on a Linkam

THMSG 600 heating-freezing system attached to a Leitz microscope. The precision of temperature measurements on the heating and cooling runs are ±2 °C and ±0.1 °C, respectively. The heating rates during observation of the homogenization temperatures (T_h) and ice-melting temperatures ($T_{m\text{-}ice}$) do not exceed 1 °C/min and 0.1 °C/s, respectively. Homogenization and trapping conditions were estimated with the HokieFlincs_H2O-NaCl spreadsheet (Steele-MacInnis et al. 2012). The summary and detailed results of fluid inclusions are shown in Table 2 and ESM Table 4, respectively. In this study, fluid inclusions were classified based on their phase states and vapor volumes at room temperature. Liquid-rich fluid inclusions (L-type) had vapor volumes of 10 to 60 % and homogenized to the liquid phase. From early to late quartz, the vapor volumes of L-type fluid inclusions decreased, concentrating at 40 to 60 % and 15 to 40 %, respectively (Table 2; ESM Table 4). Vapor-rich fluid inclusions (V-type) displayed vapor volumes of 65 to 90 % and homogenized to the vapor phase. Halite-bearing fluid inclusions (S-type) were prevalent in A2 and B1 veins. These S-type fluid inclusions were further divided into S1-type (for halite to dissolve finally) and S2-type (for bubbles to disappear finally) based on homogenization patterns, with the majority being S1-type fluid inclusions. Microthermometry results of fluid inclusion assemblages (FIAs) may have a wide range due to various reasons (Goldstein 2001; Kerkhof and Hein 2001; Fall and Bodnar 2018; Chi et al. 2021; Audétat 2023; Zhang and Audétat 2023), necessitating careful assessment of obtained data. Following the assessment criteria proposed by Goldstein (2001) and Fall and Bodnar (2018), in this study, when the majority (66.7-75 %)

of the fluid inclusions with different sizes and shapes in an FIA have T_h variations within ~35 °C, it is assumed they did not originate from heterogeneous entrapment or undergo post-entrapment modification. The detailed selection processes of FIAs and dataset assessment are shown in ESM Table 4. Primary, pseudosecondary, and secondary FIAs were tested in all types of hydrothermal quartz except for RQ_{bt}, with fifty-three primary and pseudosecondary FIAs utilized for subsequent descriptions.

Major element compositions of biotite and chlorite were obtained by electron microprobe analysis (JEOL JXA 8100). Quantitative analyses were performed using wavelength-dispersive spectrometers with an acceleration voltage of 15 kV, a beam current of 20 nA, and a 5 μm beam size. The peak counting time was 30 s for all elements and the background counting time was 10 s for the high- and low-energy background positions. The standards used were natural albite (Na), natural diopside (Si, Ca, and Mg), natural hematite (Fe), synthetic Cr_2O_3 (Cr), synthetic TiO_2 (Ti), natural orthoclase (K), natural fluorite (F), natural tugtupite (Cl), synthetic Al_2O_3 (Al), synthetic MnO (Mn), synthetic NiO (Ni), natural barite (Ba), and natural celestite (S and Sr). Data were corrected using a modified ZAF correction procedure. Detection limits are in the range of ~0.01 to ~0.06 wt%. Detailed data are shown in ESM Table 5. The biotite Ti thermometer of Henry et al. (2005) and the chlorite thermometer of Inoue et al. (2018) were used to estimate the formation temperature.

Quartz oxygen isotopes were measured in situ using the Cameca IMS-1280 SIMS. Analytical procedures were similar to the description provided by Tang et al. (2015). The

Cs^+ primary ion beam was accelerated at 10 kV, with an intensity of 2 nA and raster over a 20 μm area, to sputter quartz for oxygen isotopes analysis. The primary beam size as an ellipse was 10 × 20 μm in diameter. Oxygen isotopes were measured in multi-collector static mode using two off-axis Faraday cups, with the intensity of ^{16}O typically 2×10^9 cps. The normal electron gun was used to compensate the charging effect in the bombarding area. The Nuclear Magnetic Resonance probe was used for magnetic field control. One analysis took ~3 min composed of pre-sputtering (20 s), automatic beam centering (90 s), and integration of oxygen isotopes (16 cycles × 4 s, total 64 s). The instrumental mass fractionation factor (IMF) was corrected using Qinghu quartz with $\delta^{18}O = 8.49$ ‰ (Tang et al. 2020). Measured $^{18}O/^{16}O$ ratios were normalized to the V_{SMOW} composition ($^{18}O/^{16}O = 0.0020052$) and then corrected for the IMF. NBS-28 quartz was a second quartz standard analyzed as an unknown to ascertain the veracity of the IMF. Repeated analyses of them during analysis got a mean $\delta^{18}O$ value of 9.66±0.27 ‰ (n = 17), which is consistent with the recommended value for NBS-28 quartz (9.64±0.09 ‰; Matsuhisa 1974). The uncertainties for each analyzed spot are ~0.12 to ~0.27 ‰ (average = 0.16±0.03 ‰). Summary and detailed $\delta^{18}O$ values of different quartz types are shown in Table 3 and ESM Table 6, respectively.

Results

Texture and composition of quartz in magmatic and potassic alteration stages

At Aktogai, two types of magmatic quartz (i.e., PQ_c and PQ_r) and nine types of hydrothermal quartz (i.e., VQ_{A1}, RQ_{bt}, VQ_{A2}, RQ_{kfs}, VQ_{B1}, VQ_{BC}, VQ_C, VQ_{B2E}, and

VQ$_{B2L}$) were identified based on the quartz genesis, the type of veins and alterations, and the CL characteristics (Fig. 4).

Quartz phenocrysts found in tonalite porphyry are uncommon in rocks (~5 vol.%). They display sub-rounded shapes with diameters of ~0.5 to ~3 mm. These phenocrysts exhibit mottled gray-CL cores (PQ$_c$) surrounded by thin brighter-CL rims (PQ$_r$) (Fig. 5a). Different quartz phenocrysts show similar compositional variations (ESM Table 2), with low-Ti PQ$_c$ and high-Ti PQ$_r$ (Fig. 5b, c). However, gray-CL quartz near the rim may have high Ti contents comparable to those of PQ$_r$ (Fig. 5a, b). The average values of Ti and Al contents for PQ$_c$ are 123±18 ppm and 427±219 ppm, respectively, while for PQ$_r$, they are 165±18 ppm and 502±187 ppm, respectively (Table 1; ESM Table 2).

VQ$_{A1}$ grains, which are observed in A1 veins, exhibit homogeneous textures (CL-gray) and have fine-grained (~130 μm) or irregular morphology, distinguishing them from disseminated quartz in altered rocks (<60 μm; Fig. 6a, b). The averages of Ti and Al contents of VQ$_{A1}$ are 96±36 ppm and 174±89 ppm, respectively (Table 1). VQ$_{A2}$ grains found in A2 veins are large (up to ~250 μm) and show wavy concentric (coexisting of CL-gray and CL-gray-black quartz) or homogeneous textures (CL-gray) (Fig. 6c). The wavy concentric textures are attributed to elements diffusion after quartz crystallization (Rusk 2012; Acosta et al. 2022). The presence of K-feldspar along the VQ$_{A2}$ boundaries within A2 veins (Fig. 6c) indicates simultaneous precipitation (e.g., Chang et al. 2018). For VQ$_{A2}$, the Ti and Al contents were higher in CL-gray quartz (Ti = 74±12 ppm and Al = 161±52 ppm) compared to CL-gray-black quartz (Ti = 48±2 ppm and Al = 143±21 ppm)

(ESM Table 3). Curved grain boundaries and 120° triple junctions developed in A veins (Fig. 6b, c), indicating quartz recrystallization under high-temperature conditions (~500-600 °C; Passchier and Trouw 2005). However, the presence of wavy concentric textures in VQ_{A2} suggests that the deformation leading to quartz recrystallization ceased before the complete recrystallization (Acosta et al. 2022).

Disseminated quartz grains found in potassic altered rocks coexisted with biotite±Fe-Ti oxides (RQ_{bt}) and K-feldspar (RQ_{kfs}). RQ_{bt} grains are fine-grain (<150 μm) and show complex CL intensities, including gray, gray-black, and black (Fig. 6d). The gray-black and black CL intensities observed in RQ_{bt} may be related to quenching of CL caused by Fe diffusion (cf. Müller et al. 2010) or could have formed during chlorite replacement of hydrothermal biotite. Therefore, only CL-gray RQ_{bt} was analyzed. RQ_{kfs} grains appear as irregular shapes (<250 μm) or aggregates, exhibiting CL-gray and homogeneous textures (Fig. 6e). Both RQ_{bt} and RQ_{kfs} have comparable Ti and Al contents, with values of 49±15 ppm Ti and 144±92 ppm Al for RQ_{bt}, and 45±15 ppm Ti and 149±126 ppm Al for RQ_{kfs} (Table 1). The presence of 120° triple junctions (Fig. 6d, e) indicates that the quartz experienced high-temperature recrystallization.

VQ_{B1} in B1 veins is mostly euhedral or sub-euhedral and possesses larger grain sizes compared to VQ_{A1} and VQ_{A2}. It exhibits both oscillatory growth zones and homogeneous textures; generally, the latter is found at the center and edges of the vein, while the former is located between these areas (Fig. 7a). This phenomenon is related to varying stresses exerted on quartz with different textures (Acosta et al. 2022), resulting in various degrees of recrystallization in VQ_{B1} at different locations. K-feldspar and rutile in B1 veins either form along the VQ_{B1} boundaries or are included within the VQ_{B1} grains (Fig. 7a, c), indicating simultaneous precipitation. Some molybdenite near the vein's edge is directly in contact with VQ_{B1} (Fig. 7a), suggesting co-precipitation. Except for bright-CL areas of VQ_{B1} with oscillatory growth zones, trace elements among quartz with different textures show no obvious difference. The averages of Ti and Al contents for these quartz are 23±6 ppm and 96±47 ppm, respectively (Table 1). In VQ_{B1} with oscillatory growth zones, bright-CL areas have higher Ti contents than gray-CL areas (Fig. 8a). Given that the bright-CL areas have a width of <100 μm and the in-situ oxygen isotopes in these zones are consistent (Table 3), the variations in Ti and Al contents within the oscillatory growth zones can be attributed to changes in growth rates and/or disequilibrium precipitation (Barker and Cox 2011; Acosta et al. 2020).

VQ_{BC} mainly occurred in B1 veins, displaying homogeneous textures and a black CL color. They crosscut early quartz grains either as irregular veins (Fig. 7a) or precipitated along the boundaries of early quartz grains and microfractures (Fig. 7b, d). Sulfides co-precipitated with VQ_{BC} (Fig. 7a, b), while chlorite, white mica, and early quartz fragments are also observed within VQ_{BC}. The averages of Ti and Al contents of VQ_{BC} are 17±4 ppm and 100±98 ppm, respectively (Table 1), which are lower than those of VQ_{B1} (Fig. 8b). VQ_{C}, found in C veins, exhibits black-gray CL with oscillatory growth zones or homogeneous black CL. The black CL VQ_{C} crosscut the black-gray CL VQ_{C} (Fig. 7d), indicating that the latter predated the former. Sulfides directly contact both types of VQ_C, and chlorite and fluorite are also observed. Unlike VQ_{BC}, VQ_C displays a flatter contact interface with early quartz grains, with the black-gray CL VQ_C growing toward the interior along the boundary of the early quartz (Fig. 7d). VQ_C has the lowest Ti content with an average of 8±3 ppm (Fig. 8c; Table 1). The absence of recrystallization in both VQ_{BC} and VQ_C suggests that they were not affected by high-temperature recrystallization.

One type of quartz (i.e., VQ_{B2}), occurring in B2 veins, exhibits surprisingly higher Ti contents compared to VQ_{B1} (Table 1). VQ_{B2} is further divided into VQ_{B2E} and VQ_{B2L} based on their CL features (Fig. 9). VQ_{B2E} shares similar morphology, grain size, and textural features with VQ_{B1}, with averages Ti and Al contents of 54±13 ppm and 93±76 ppm, respectively (Table 1). Conversely, VQ_{B2L} displays gray-black CL quartz with mottled and wavy concentric textures, associated with sulfide centerlines, and shows incompletely dissolved VQ_{B2E} (Fig. 9). The Ti (33±13 ppm) and Al (71±10 ppm) contents of VQ_{B2L} are lower than VQ_{B2E} (Fig. 8d) but higher than VQ_{BC} and VQ_C (Fig. 10a; Table 1). In general, later veins tend to exhibit more planar characteristics compared to earlier ones (Sillitoe 2010; Monecke et al. 2018), and the Ti content of later quartz typically decreases compared to earlier ones (Rottier and Casanova 2021; Gao et al. 2022). However, the observation regarding the Ti content in VQ_{B2} compared to VQ_{B1} and VQ_{BC} (Fig. 10a), despite the expected trends in planarity and T_h data (Table 2), suggests a unique geological scenario. The presence of rutile in fluid inclusions, veins, and altered rocks (ESM Fig. 3), resulting in an α_{TiO2} value of 1, suggests that the elevated Ti content in VQ_{B2} is not influenced by the α_{TiO2} in the fluid. The two proposed explanations for this phenomenon are both plausible: (1) VQ_{B2} may have been formed in a different magmatic-hydrothermal event, leading to significantly different Ti contents in the involved fluids; (2) VQ_{B2} may have experienced lower pressures than VQ_{B1}. Subsequent discussion does not involve VQ_{B2} because they are from only one sample and their genesis is unclear.

The blackest CL quartz precipitated along microfractures and commonly appeared in different vein types. They intersect VQ_{BC} and VQ_C (ESM Fig. 4). No valid data were obtained for this quartz type because it is too thin.

Overall, there is a discernible trend from early (VQ_{A1} to RQ_{kfs}) to late (VQ_{B1} to VQ_C) quartz, where CL intensities decrease alongside the contents of Ti and Al within quartz (Fig. 10a, b). The Al/Ti ratios, however, exhibit an increase over time (Fig. 10c). Most quartz shows relatively constant Ti contents within the same quartz type. The decline in Ti content in quartz from early to late is linked to fluid cooling, given that Ti content in quartz is positively correlated with formation temperatures (Rottier and Casanova 2021; Gao et al. 2022), a conclusion supported by our fluid inclusion data. The Al contents in various quartz types decrease and show large variations in late quartz (Fig. 10b), with Al/Ti ratios gradually increasing from early to late (Fig. 10c). These trends align with the transition from feldspar-stable to feldspar-destructive alterations (Rottier and Casanova 2021): early quartz precipitates under higher-temperature conditions where K-feldspar remains stable, whereas late quartz forms under lower-temperature conditions resulting in the decomposition of K-feldspar (replaced by white mica and chlorite), consequently increasing the Al/Ti ratio in the quartz.

Fluid inclusions

In this study, fluid inclusion assemblages (FIAs) are strictly defined based on petrographic observations, following the criteria outlined by Roedder (1984) and Goldstein (2001), i.e., fluid inclusion groups were trapped simultaneously and formed along growth zones or fractures (Fig. 11a, b, d, e, f; ESM Fig. 5). Although fluid inclusions clusters are not strictly FIAs, as some quartz types exclusively contain this type of fluid inclusion (Fig. 11c, g, h), we regarded them as analogous to FIAs when the petrographic observations of quartz are texturally homogeneous, microfractures absent, and the vapor volumes of the fluid inclusions similar (cf. Chang et al. 2018). Each FIA is used as one data.

Numerous studies have investigated the origin of brine fluid inclusions that homogenize via halite dissolution (i.e., S1-type fluid inclusion in this study). Commonly found in porphyry systems, these fluid inclusion result from heterogeneous trapping, post-entrapment modification, or trapping a single-phase liquid under high-pressure conditions (Becker et al. 2008; Lecumberri-Sanchez et al. 2012, 2015; Audétat 2023). In this study, reliable petrographic evidence indicates the presence of V-type fluid inclusions coexisting with the S1-type fluid inclusions (i.e., boiling FIAs). However, the ranges in T_h and halite-melting temperatures of these S1-type fluid inclusions are highly variable (Fig. 12a; ESM Table 4), suggesting post-entrapment modification (Becker et al. 2008;

Lecumberri-Sanchez et al. 2012). Consequently, these data were discarded in subsequent reports and discussions.

The first ice-melting temperatures of the valid FIA data obtained exhibit no significant variation, ranging from -52 to -29 °C, implying the presence of elements beyond NaCl and KCl in the fluids (Crawford, 1981). Laser Raman analysis revealed the presence of CO_2, calcite, anhydrite, hematite, chalcopyrite, and rutile within the fluid inclusions (Fig. 12c-f). CO_2 and anhydrite were observed in VQ_{B1}, while chalcopyrite predominated in VQ_{B2L}, VQ_{BC}, and VQ_{C}. Calcite, hematite, and rutile were found in all quartz types, suggesting the presence of Ca, Fe, Cu, and Ti ions in the fluid. CO_2-bearing fluid inclusions were exclusively identified through Raman spectroscopy, indicating a minor component concentration ($\leqslant$~2 mol%; Rosso and Bodnar 1995).

The examination of FIAs in quartz specimens from various samples reveals a spectrum of thermodynamic properties (Fig. 12b). In VQ_{A1}, FIAs exhibit L-type characteristics, with T_h of 441 to 456 °C, salinities of 6.8 to 7.9 wt%, homogenization pressures of 400 to 449 bar, and densities of 0.48 to 0.52 g/cm^3. Conversely, VQ_{A2} predominantly shows boiling assemblages, with T_h of 398 to 412 °C. Salinities of V-type and S2-type fluid inclusions are 4.7 to 6.1 wt% and 45.0 to 45.9 wt%, respectively. Homogenization pressures for V-type and S2-type fluid inclusions are 279 to 328 bar and 173 to 194 bar, respectively, while their fluid densities are 0.51 to 0.56 g/cm^3 and 1.05 to 1.06 g/cm^3, respectively. Additionally, a few L-type FIAs were found in VQ_{A2}, characterized by relatively high T_h (~422 °C) and homogenization pressures (335 to 336 bar), with salinities of 6.9 to 7.6 wt.%. RQ_{kfs} includes L-type and V-type FIAs, with similar T_h, salinities, and homogenization pressures as the boiling FIAs in VQ_{A2}, ranging from 390 to 413 °C, 6.3 to 6.6 wt%, and 249 to 312 bar, respectively. In VQ_{B1}, L-type FIAs predominate, but numerous V- and S-type fluid inclusions were also observed. There are no obvious differences in the types and properties of FIAs in VQ_{B1} with different textures. Homogenization temperatures, salinities, and homogenization pressures of L-type FIAs in VQ_{B1} are lower than those in VQ_{A1} and VQ_{A2}, with 345 to 390 °C, 2.0 to 6.1 wt%, and 152 to 253 bar, respectively. The fluid densities for this quartz type range from 0.55 to 0.65 g/cm^3, higher than those in VQ_{A1} and VQ_{A2}. V-type fluid inclusions found in VQ_{B1} have slightly higher T_h than L-type fluid inclusions (Fig. 12b; ESM Table 4). VQ_{B2E} exclusively contains L-type fluid inclusions, with T_h, salinities, and homogenization pressures of 303 to 328 °C, 3.2 to 4.0 wt%, and 88 to 123 bar, respectively. In VQ_{B2L}, VQ_{BC}, and VQ_C, which co-precipitate with sulfides, the FIAs are L-type. FIAs in VQ_{B2L} have T_h and salinities of 282 to 296 °C and 3.3 to 4.4 wt%, while those in VQ_{BC} are 322 to 341 °C and 1.7 to 4.0 wt%, respectively. FIAs in VQ_C exhibit the lowest T_h (264 to 279 °C) and salinities (2.6 to 3.5 wt%). Fluids in VQ_{B2L}, VQ_{BC}, and VQ_C have high densities, ranging from 0.66 to 0.80 g/cm^3.

Boiling FIAs can provide accurate trapping conditions, but many FIAs in this study need pressure correction as they did not record boiling processes. Based on the denudation depth, sample elevation, and rock behavior during vein formation, a pressure correction of 500 bar was applied for the A1 and A2 veins and potassic altered rocks, and

200 bar for other vein types (see section "Trapping pressures and emplacement depth at Aktogai" for the detailed discussion about pressure). Following the correction, the temperatures for VQ_{A1}, VQ_{A2}, RQ_{kfs}, VQ_{B1}, VQ_{BC}, VQ_C, VQ_{B2E}, and VQ_{B2L} are 467-470 °C, 438-457 °C, 433-452 °C, 351-380 °C, 332-347 °C, 276-291 °C, 314-337 °C, and 294-307 °C, respectively (ESM Table 4). It's worth noting that these temperatures are approximations due to fluctuations in the formation pressure of the porphyry system (between lithostatic and hydrostatic pressures), especially during the transition stage.

Mineral composition-based thermometers

Biotite associated with RQ_{bt} is Mg-biotite (ESM Fig. 6a), with Mg/(Mg+Fe) ratios and Ti atoms ranging from 0.58 to 0.61 (ESM Fig. 6b) and 0.06 to 0.07, respectively. Estimated temperatures based on the biotite Ti thermometer range from 505 to 540 °C (ESM Table 5). Chlorite associated with VQ_{BC} and VQ_C fall within the brunsvigite fields (ESM Fig. 6c), with VQ_C showing higher Si and lower Al atoms compared to VQ_{BC} (ESM Fig. 6d). Estimated temperatures for chlorite associated with VQ_{BC} and VQ_C range from 307 to 320 °C and 216 to 261 °C, respectively (ESM Table 5).

Crystallization temperatures were estimated using the hydrothermal quartz data and Ti-in-quartz thermometers. The data for the bright CL bands in VQ_{B1} with growth zones and the gray-black CL parts in VQ_{A2} with wavy concentric textures were excluded due to potential precipitation under Ti disequilibrium conditions (Acosta et al. 2022). Rutile's ubiquitous presence (Figs. 7a, 12e; ESM Fig. 3) indicates an α_{TiO2} value of 1 in the hydrothermal fluid. Similar to the pressures used for pressure correction for T_h, the pressure used to estimate the temperatures of VQ_{A1}, RQ_{bt}, VQ_{A2}, and RQ_{kfs} is 500 bar, while for other quartz types is 200 bar (ESM Table 3). Calculation results show that the highest results are obtained by the method of Huang and Audétat (2012) and the lowest by the method of Zhang et al. (2020), but all results are higher than those from chlorite and fluid inclusions (Fig. 13; ESM Fig. 7). Petrologic evidence suggests quartz co-precipitated with analyzed biotite, chlorite, and fluid inclusions, aiding in identifying the most suitable Ti-in-quartz thermometer for hydrothermal conditions. The diagram illustrates the method of Zhang et al. (2020) as most analogous below 400 °C ($\Delta T <$ ~-30 °C; Fig. 13). Above 400 °C, all results diverge from those obtained by independently ($\Delta T > \pm 50$ °C; Fig. 13). This discrepancy may be explained by (1) frequent pressure changes result in inaccurate temperatures and pressures obtained by fluid inclusions and (2) variable growth rates and potential disequilibrium precipitation of hydrothermal quartz (Huang and Audétat 2012; Acosta et al. 2022). As the result of Zhang et al. (2020) is similar to those of FIAs, we use its results and formation temperatures of VQ_{A1}, RQ_{bt}, VQ_{A2}, RQ_{kfs}, VQ_{B1}, VQ_{BC}, VQ_{C}, VQ_{B2E}, and VQ_{B2L} are 561±42 °C, 494±31 °C, 537±18 °C, 488±27 °C, 396±20 °C, 373±18 °C, 322±28 °C, 466±22 °C, and 422±30 °C, respectively. The temperature obtained by the Ti-in-quartz thermometer served as the maximum formation temperature of the hydrothermal quartz (Huang and Audétat 2012).

In-situ quartz oxygen isotopes

VQ_{B1} grains from different veins or the same vein but with different textures show slight variations in $\delta^{18}O_{Qz}$ values (Table 3; Fig. 14). $\delta^{18}O_{Qz}$ values of VQ_{B1} with oscillatory growth zones in the quartz-K-feldspar-molybdenite vein display a narrow range, with an average of 9.21±0.16 ‰. VQ_{B1} grains in the quartz-K-feldspar-chalcopyrite vein have slightly lower $\delta^{18}O_{Qz}$ values, with averages of 8.84±0.11 ‰ for those with oscillatory growth zones and 8.96±0.10 ‰ for those with homogeneous or mottled textures.

Before using $\delta^{18}O_{Qz}$ to calculate $\delta^{18}O_{fluid}$, it is crucial to ensure that the quartz crystallized under isotopic equilibrium conditions. Isotopic equilibrium is reached when the time for the quartz to precipitate exceeds the time required for quartz and fluids to achieve isotopic equilibrium (Cole et al. 1992). Previous studies indicated that it takes more than hundreds of years to form quartz with hundreds of μm (Mercer et al. 2015), which is long enough for quartz and fluids to achieve isotopic equilibrium (<20 years; Li et al. 2018c). Although rapid quartz growth due to high fluid temperatures can lead to local isotopic heterogeneity, the analyzed quartz grains in this study are >500 μm and exhibit concentrated $\delta^{18}O_{Qz}$ values in each sample, also indicating isotopic equilibrium conditions. Factors like mineral precipitation, dissolution-reprecipitation, and microfractures can also influence $\delta^{18}O_{Qz}$ values (Elsenheimer and Valley 1993; Valley and Graham 1996). However, as the tested veins share the same silicate assemblage (e.g., K-feldspar), mineral assemblages likely have minimal effects on $\delta^{18}O_{Qz}$ values. Moreover, dissolution-reprecipitation and microfractures observed through polarized light and CL were avoided during analysis. Hence, the $\delta^{18}O_{Qz}$ differences between quartz in the two veins likely reflect source differences in mineralizing fluids.

Based on the oxygen isotope fractionation equation between quartz and fluid, and using corrected temperatures obtained by FIAs, the average $\delta^{18}O_{fluid}$ values for the different VQ_{B1} are as follows: 4.70±0.17 ‰ for oscillatory growth zones in the quartz-K-feldspar-molybdenite vein, 4.10±0.11 ‰ for oscillatory growth zones in the quartz-K-feldspar-chalcopyrite vein, and 4.22±0.11 ‰ for homogeneous textures in the quartz-K-feldspar-chalcopyrite vein (Table 3). Considering that late-stage fluids at Aktogai exhibit low salinity and low CO_2 contents (Li et al. 2018b), magmatic and meteoric water were used as the two end members to estimate the contribution of magmatic water in the fluid. The average oxygen isotopes of magmatic fluids ($\delta^{18}O_{magmatic}$) estimated from zircon oxygen isotopes (Shen et al. 2018) and the method of Krylov et al. (2002) is 6.31±0.23 ‰. As there are no studies on the $\delta^{18}O$ values of meteoric water ($\delta^{18}O_{meteoric}$) at ~330 Ma at Aktogai, a $\delta^{18}O_{meteoric}$ value of -8.9 ‰ was assumed based on present $\delta^{18}O_{meteoric}$ values (Terzer et al. 2013), paleo-latitude (~25° N; Choulet et al. 2011), and tectonic settings (Cao et al. 2016). Therefore, the percentage contributions of magmatic water in the fluid of B1 veins are 86 to 89 vol% (Table 3).

Discussion

Trapping pressures and emplacement depths at Aktogai

The ore-related intrusion of PCD results from the rapid emplacement of magma within the middle to upper crustal magma chamber (Sillitoe 2010; Richards 2011). The depth of emplacement influences both mineral assemblages and the nature and evolution of mineralizing fluids (Murakami et al. 2010; Monecke et al. 2018). Despite its significance, determining trapping pressures during mineralization processes is difficult.

Recent advancements in Ti-in-quartz barometers have demonstrated promising capabilities in estimating pressures within magmatic systems (e.g., Audétat 2013; Müller et al. 2018; Huang et al. 2020), particularly in porphyry systems. These barometers offer comparable uncertainties to conventional mineral barometers (e.g., amphibole, Ridolfi and Renzulli, 2012; biotite, Uchida et al. 2007), with the added advantage of quartz being more resistant to hydrothermal alterations. In this study, Ti-in-quartz barometers were employed to estimate the formation pressure of magmatic quartz. Previous studies indicate that the core-rim CL texture is common in volcanic rocks and ore-related intrusions in PCDs, with high-Ti rims forming under conditions of increased temperature or decreased pressure, accompanied by changes in α_{TiO2} (Audétat 2013; Pamukcu et al. 2016; Huang et al. 2020). At Aktogai, quartz phenocrysts in ore-related tonalite porphyry exhibit the core-rim CL texture (Fig. 5a). Given the absence of mafic magma mixing during deposit formation (Cao et al. 2016), the PQ_r at Aktogai is likely associated with a rapid decrease in pressure during emplacement. Consequently, pressures estimated from PQ_c and PQ_r should correspond to the formation pressure of the middle to upper crustal magma chamber and the emplacement pressure of the tonalite porphyry, respectively. For PQ_c, despite variations in α_{TiO2} in the magma (Fonseca Teixeira et al. 2024), it is assumed to be 0.6 (cf. Hayden and Watson, 2007) for estimating formation pressure because the tonalite porphyry is homogeneous and contains magmatic titanite and ilmenite (Cao et al.

2016). The highest zircon crystallization temperature (T_{zrn} = 806 °C; data from Shen et al. 2015) was used because quartz grains occurred as mineral inclusions in zircon grains (ESM Fig. 8), indicating that quartz formed earlier than or simultaneously with zircons. Therefore, the average P_{T10}, P_{H12}, and P_{Z20} of PQ_c are 8.6±0.8 kbar, 1.9±0.5 kbar, and 4.3±1.4 kbar, respectively (ESM Table 2). Assuming a lithostatic pressure of 265 bar/km, estimated paleo-depths are 32.5±3.0 km, 7.2±1.9 km, and 16.2±5.3 km, respectively. For the PQ_r, as magma cools during emplacement due to heat exchange with wall rocks, its formation temperature lies between the highest T_{zrn} and the granodiorite solidus temperature. Considering fluid inclusion data obtained in this study (>~1.9 km for A1 veins and ~1.7-2.0 km for A2 veins; see the following paragraph for a detailed discussion), geological reconstructions (~1.5-2.0 km erosion depths for the Aktogai deposit; Zvezdov et al. 1993), and the sample elevation (~400-450 m), the paleo-depth of tonalite porphyry ranges from ~1.9 to ~2.4 km. Under lithostatic pressure, this corresponds to pressures of ~500 to ~640 bar and granodiorite solidus temperatures of ~745-755 °C (average = 750 °C). Additionally, given the elevated oxygen fugacity at Aktogai (Shen et al. 2015; Li et al. 2018a), the α_{TiO2} would increase as magma cools (Ghiorso and Gualda 2013). As magmatic rutile is absent and α_{TiO2} for felsic magmas typically falls within 0.6-0.9 (Ghiorso and Gualda 2013), the highest α_{TiO2} at Aktogai should be less than 0.9. The pressure estimated by the Ti-in-quartz barometer increases with temperature and α_{TiO2}, thus the formation pressure of tonalite porphyry should be higher than that estimated from the lowest temperature (750 °C) and α_{TiO2} (0.6).

Consequently, the average P_{T10}, P_{H12}, and P_{Z20} of PQ_r are >4.9±0.5 kbar, >0.4±0.1 kbar, and >1.1±0.3 kbar, respectively (ESM Table 2), corresponding to paleo-depths of >18.5±1.9 km, >1.5±0.4 km, and >4.2±1.1 km, respectively. Combining fluid inclusion data with geological information (i.e., denudation depth and sample elevation), the results of P_{H12} are reasonable. Results of P_{T10} showing the highest pressures may be because this method applies to conditions of 5-20 kbar. This range does not typically align with the formation of silicic magmas, which usually occur under conditions of <5 kbar (Wilke et al. 2017). Similarly, the high paleo-depths estimated using the P_{Z20} for PQ_r may be due to the method's focus on high-silica magmas (Zhang et al. 2020).

Fluid inclusion studies are generally used to infer pressures and formation depths in hydrothermal systems (e.g., Li et al. 2018c; Bain et al. 2022; Schirra et al. 2022), especially the boiling FIAs that can provide accurate trapping conditions. In this study, the L-type fluid inclusions within A1 veins recorded the fluid's temperature and density at ~470 °C and ~0.50 g/cm^3, respectively. These values indicate a minimum pressure requirement of ~500 bars for the formation of this single-phase fluid in the H_2O-NaCl system (Bischoff 1991). Given that the A veins in the porphyry system form under lithostatic pressure (Monecke et al., 2018), and considering the discontinuous or irregular walls and thin widths observed in the analyzed A1 veins (Figs. 3b, 6b), the estimated formation depth of the A1 veins exceeds ~1.9 km based on lithostatic pressure. Unlike A1 veins, A2 and B1 veins exhibit widespread development of boiling FIAs. S2-type fluid inclusions within A2 veins give pressures of ~170-200 bar and formation temperatures of

~390-420 °C (ESM Table 4). Given the presence of L-type FIAs with higher T_h (~422 °C) and homogenization pressures (~335 bar) in this vein (ESM Table 4), along with the observation of relatively straight walls and broad widths in the analyzed A2 veins (Fig. 6a, c), the pressure during vein formation varied between lithostatic and hydrostatic pressures (Monecke et al. 2018) and that these boiling FIAs are more likely to form at hydrostatic pressure. Based on hydrostatic pressure considerations, the A2 vein is estimated to have formed at depths of ~1.7-2.0 km. For the B1 vein, although we do not obtain valid boiling FIA data (as all S-type fluid inclusions are S2-type, suggesting that the boiling FIAs affected by post-entrapment modification; ESM Table 4), the B1 veins generally have flat walls and broad widths (Fig. 3d-f), the quartz within them develops growth zones (Fig. 7), and the T_h of L-type FIAs (~350 to <~390 °C) is distinctly lower than that of the V-type fluid inclusions (~380-410 °C) in the boiling FIA (ESM Table 4). These observations suggest several key points: firstly, the fractures likely formed over an extended time, allowing quartz to develop oscillatory growth zones; secondly, both the tested B1 veins and the quartz within them avoided high-temperature recrystallization; thirdly, their formation is more likely associated with brittle behavior and hydrostatic pressure (Fournier, 1999; Monecke et al., 2018). Consequently, the L-type fluid inclusion in the B1 vein shows homogenization pressures (i.e., minimum trapping pressure) of ~170-240 bar, corresponding to paleo-depths of ~1.7-2.4 km. Additionally, the vertical distribution of different vein types and quartz at Aktogai shows no significant variation, suggesting uniform formation depths of ~1.7-2.4 km.

Overall, the estimated emplacement depths of the tonalite porphyry and veins, derived from Ti-in-quartz barometers and FIAs, closely align with estimations based on deposit denudation, sample elevation, and previous studies by Li et al. (2012), utilizing $^{40}Ar/^{39}Ar$ ages of amphibole, biotite, K-feldspar, and apatite fission-track ages (>2 km but <~5 km). This convergence of data suggests the reliability of the pressure and depth estimations. Accordingly, the shallow magma chamber of the Aktogai system is estimated to have formed at ~1.9±0.5 kbar (~7.2±1.9 km), while the emplacement depths of tonalite porphyry and formation depths of veins are ~1.7-2.4 km. These depths are consistent with those of Mesozoic and Cenozoic PCDs worldwide, typically ranging from ~5 to ~15 km for shallow magma chambers and <5 km for ore-related intrusions (Cloos, 2001; Sillitoe, 2010; Richards, 2011).

Fluid evolution at Aktogai

Combining quartz textures, trace elements, and in-situ oxygen isotopes, as well as FIA data, we traced the fluid evolution process at Aktogai.

The earliest vein identified in this study, the A1 vein, exhibited the highest temperature (~470-560 °C). The presence of solely L-type fluid inclusions in A1 veins suggests that the earliest fluid was single-phase (Fig. 15a). Quartz precipitation in A1 veins suggests a decrease in SiO_2 solubility in the evolving fluid. Considering the pressure-temperature conditions of tonalite porphyry and A1 veins, it is probable that A1 veins formed during the cooling of ascending fluids (Fig. 15a). The increasing pressure and quasi-isobaric cooling processes were not pronounced at this period due to the absence of dissolution textures and quartz-free veins. Biotite, magnetite, and minor quartz, observed as replacements of mafic minerals under high temperatures (~490-540 °C; ESM Tables 3, 5), also formed during this period.

The presence of irregular K-feldspar-dominated A2 veins at Aktogai suggests that SiO_2 solubility in the fluid remained unchanged during vein formation. These veins formed through quasi-isobaric cooling, where SiO_2 solubility increases with decreasing temperature (Fig. 15a). As tonalite porphyry is withdrawn over time, the host rock cools, transitioning from ductile to brittle once temperatures drop to ~450 °C, accompanied by a rapid decrease in pressure from lithostatic to hydrostatic pressure (Fournier, 1999; Monecke et al., 2018). The widespread development of boiling FIAs in quartz-dominated A2 veins suggests formation during fluid boiling, with a few L-type FIAs with higher T_h indicating single-phase fluids before boiling (Fig. 15b). The temperature and pressure transition between L-type FIAs in A1 veins (~470-560 °C, >~500 bar) and boiling FIAs in quartz-dominated A2 veins (~400 °C, ~200 bar) reflect the host rock's transition from ductile to brittle behavior, and the transition from lithostatic to hydrostatic pressures leads to fluid boiling. Disseminated K-feldspar and quartz with similar temperatures (~430-490 °C; Table 2) to A2 veins also formed during this period. A veins intersect each other (Fig. 3b), and extensive quartz recrystallization (Fig. 6) resulted from repeated cleavage and healing of the intrusion (Weis et al. 2012). Negligible sulfides occurred in A veins because high temperatures (>400 °C) result in high solubility of Cu and Mo in the fluid (Cao 1989; Zhong et al. 2015), and SO_2 in the fluid not yet converted to S^{2-} and

SO_4^{2-} by disproportionation (Richards 2011). Minor chalcopyrite, which precipitates in altered rocks or contact zones between veins and host rocks, results from water-rock reactions between mineralizing fluids and host rocks. This because mafic minerals, feldspar, and carbonate in host rocks can buffer mineralizing fluids to readily precipitate sulfides (Porter 2016; Park et al. 2021).

B veins exhibit planar walls. VQ_{B1} primarily contains L-type fluid inclusions, yet boiling assemblages (V-type fluid inclusions in boiling FIAs have higher T_h than L-type FIAs; ESM Table 4) were also present, indicating that the intermediate-temperature fluid (~350-400 °C; Table 2) was within the two-phase field but intersected the single-phase field with cooling (Fig. 15b). B1 veins have comparable homogenization pressures (~170-240 bar) to A2 veins, suggesting possible formation through quasi-isobaric cooling under open-system conditions within the L+V field (Fig. 15b). The involvement of minor meteoric water (~11-14 %; Table 3) could be linked to fractures' development under the open system (Fekete et al. 2016).

Retrograde quartz solubility occurs at ~375-400 °C under hydrostatic conditions based on the model of Monecke et al. (2018). Under such conditions, quasi-isobaric cooling of single-phase fluids could result in quartz dissolution or the formation of quartz-free veins (Fig. 15b). At Aktogai, previously formed quartz shows dissolution characteristics (Figs. 7, 9) suggesting that the fluid entered the retrograde quartz solubility field. VQ_{BC}, VQ_C, and sulfides precipitated within the voids and microfractures of the dissolved quartz grains. The exclusive presence of L-type fluid inclusions in these quartz types indicates that the fluid remained in the single-phase field. Both VQ_{BC} and VQ_C are related to Cu mineralization. VQ_{BC} typically shows more irregular occurrences (e.g., irregular shapes or veinlets; Fig. 7) and contains less quartz but records higher temperatures (~330-370 °C) compared to VQ_C. The formation of VQ_{BC} aligns with that of quartz co-precipitated with Cu-Fe sulfides found in other PCDs (e.g., Müller et al. 2010; Tsuruoka et al. 2021; Schirra et al. 2022). This formation typically occurs near the retrograde quartz solubility field (Fig. 15b), resulting in minimal quartz precipitation. However, the presence of minor CO_2 ($\leqslant$~2 mol%; Fig. 12c) in the mineralizing fluid reduces the impact of retrograde quartz solubility and moves it towards lower temperatures (Monecke et al. 2019), thus facilitating the formation of quartz-dominated sulfide-bearing veinlets (Fig. 7a). VQ_C forms at relatively low temperatures (~275-320 °C), where the quartz solubility decreases with decreasing temperature (Fig. 15b), leading to substantial quartz precipitation. The increase of Al/Ti ratios observed in VQ_{BC} and VQ_C (Fig. 10c) indicates increased H^+ metasomatism (Rottier and Casanova 2021). Sulfide precipitation primarily occurs in veins either as disseminated forms or symmetrically in the center (Figs. 7b, d, 9), with some sulfides (especially molybdenite, often coexisted with white mica) also precipitating at contact zones between veins and host rocks (Fig. 7a). Fluid cooling should play an important role on sulfide precipitation because the decrease of temperature will result in Cu and Mo precipitation (Cao 1989; Redmond et al. 2004; Rempel et al. 2008). Similar to the sulfide in A veins, water-rock reactions that form white mica and consume H^+ atoms in the fluid are crucial for molybdenite precipitation near host rocks. Notably, boiling FIAs are absent in quartz precipitated with sulfides.

Implications

The timing and temperature of Cu-Fe sulfide precipitation in PCDs remain controversial. Some studies indicate a close association between Cu-Fe sulfide and the A vein and potassic alteration, typically occurring at temperatures exceeding ~400 °C (Hemley et al. 1992; Rusk et al. 2008). Conversely, other studies suggest a linkage between Cu-Fe sulfide and later quartz, characterized by darker CL color and lower temperatures (~300-450 °C), often intersecting earlier quartz (Müller et al. 2010; Tsuruoka et al. 2021; Schirra et al. 2022). Recently, Cernuschi et al. (2023) proposed a model suggesting that Cu-Fe sulfide precipitation primarily occurs during high-temperature A veins and potassic alteration, with later quartz introducing minor percentages of Cu-Fe sulfides at intermediate temperatures, possibly due to remobilization-reprecipitation processes. Our study at Aktogai focuses on elucidating the formation sequence of hydrothermal quartz and determining the timing and temperature of metal precipitation. We observed that earlier quartz (VQ_{A1} to RQ_{kfs}) lacks direct contact with Cu-Fe sulfides and exhibits few chalcopyrite daughter minerals in hosted fluid inclusions, implying rare Cu-Fe sulfide precipitation during high-temperature conditions. In contrast, fluid inclusions containing chalcopyrite begin to increase in VQ_{B1} and are prevalent in later quartz (VQ_{BC} and VQ_{C}; Figs. 4, 12f), which directly contact with or envelope Cu-Fe sulfides (Figs. 7, 9). Parts of later quartz were formed as microfractures or along grain boundaries, which may follow the model proposed by Cernuschi et al. (2023). More later quartz, however, crosscuts early quartz as veinlets or veins (Figs. 7a, d, 9), a phenomenon unlikely to result from volume contraction in early quartz. This observation suggests simultaneous precipitation of later quartz and sulfides. Therefore, this study supports the idea that Cu-Fe sulfides are closely related to later quartz formed under intermediate-temperature conditions.

Acknowledgments

We would like to thank Ke Huang and Xinghui Li for numerous discussions. Sincere thanks to Matthew Steele-MacInnis, Wyatt Bain, and Mitchell Bennett for their constructive comments and editing on this manuscript. This study was granted by the International Partnership Program of the International Cooperation Bureau, the Chinese Academy of Sciences (Grant No. 132A11KYSB20190070), the National Natural Science Foundation of China (42002092), and the China Postdoctoral Science Foundation (Grant No. 2019M660787).

References cited

Acosta, M.D., Watkins, J.M., Reed, M.H., Donovan, J.J., and Depaolo, D.J. (2020) Ti-in-quartz: Evaluating the role of kinetics in high temperature crystal growth experiments. Geochimica et Cosmochimica Acta, 281, 149-167.

Acosta, M.D., Reed, M.H., and Watkins, J.M. (2022) Quartz vein formation and deformation during porphyry Cu deposit formation: A microstructural and geochemical analysis of the Butte, Montana, ore deposit. Lithosphere, 2022, 3196601.

Ancey, M., Bastenaire, F., and Tixier, R. (1978) Applications of statistical methods in microanalysis. In F. Maurice, Eds., Proc. Summer School St. Martin-d'Herres. Les Editions de Physique, Orsay, p. 319-343.

Audétat, A. (2013) Origin of Ti-rich rims in quartz phenocrysts from the Upper Bandelier Tuff and the Tunnel Spring Tuff, southwestern USA. Chemical Geology, 360-361, 99-104.

Audétat, A., Garbe-Schönberg, D., Kronz, A., Pettke, T., Rusk, B., Donovan, J.J., and Lowers, H.A. (2014) Characterisation of a natural quartz crystal as a reference material for microanalytical determination of Ti, Al, Li, Fe, Mn, Ga and Ge. Geostandards and Geoanalytical Research, 39, 171-184.

Audétat, A. (2023) A Plea for More Skepticism Toward Fluid Inclusions: Part II. Homogenization via Halite Dissolution in Brine Inclusions from Magmatic-Hydrothermal Systems Is Commonly the Result of Postentrapment Modifications. Economic Geology, 118, 43-55.

Bain, W.M., Lecumberri-Sanchez, P., Marsh, E.E., Steele-MacInnis, M., 2022. Fluids and Melts at the Magmatic-Hydrothermal Transition, Recorded by Unidirectional Solidification Textures at Saginaw Hill, Arizona, USA. Economic Geology, 117, 1543-1571.

Barker, S.L.L., and Cox, S.F. (2011) Oscillatory zoning and trace element incorporation in hydrothermal minerals: insights from calcite growth experiments. Geofluids, 11, 48-56.

Becker, S.P., Fall, A., and Bodnar, R.J. (2008) Synthetic Fluid Inclusions. XVII. PVTX Properties of High Salinity H2O-NaCl Solutions (>30 wt % NaCl): Application to Fluid Inclusions that Homogenize by Halite Disappearance from Porphyry Copper and Other Hydrothermal Ore Deposits. Economic Geology, 103, 539-554.

Bischoff, J.L. (1991) densities of liquids and vapors in boiling NaCl-H_2O solutions: A PVTX summary from 300 to 500 °C. American Journal of Science, 291, 309-338.

Bouzari, F., and Clark, A.H. (2006) Prograde evolution and geothermal affinities of a major porphyry copper deposit: The Cerro Colorado Hypogene Protore, I Región, Northern Chile. Economic Geology, 101, 95-134.

Burke, E.A.J. (2001) Raman microspectrometry of fluid inclusions. Lithos, 55, 139-158.

Cao, M.J., Li, G.M., Qin, K.Z., Evans, N.J., and Seitmuratova, E. (2016) Assessing the magmatic affinity and petrogenesis of granitoids at the giant Aktogai porphyry Cu deposit, Central Kazakhstan. American Journal of Science, 316, 614-668.

Cao, X.Y. (1989) Solubility of molybdenite and the transport of molybdenum in hydrothermal solutions. Ph.D. thesis, Iowa State University, 103 pp.

Cernuschi, F., Dilles, J.H., Osorio, J., Proffett, J.M., and Kouzmanov, K. (2023) A reevaluation of the timing and temperature of copper and molybdenum precipitation in porphyry deposits. Economic Geology, 118, 931-965.

Chang, J., Li, J.W., and Audétat, A. (2018) Formation and evolution of multistage magmatic-hydrothermal fluids at the Yulong porphyry Cu-Mo deposit, eastern Tibet:

Insights from LA-ICP-MS analysis of fluid inclusions. Geochimica et Cosmochimica Acta, 232, 181-205.

Chen, X.H., Seitmuratova, E., Wang, Z.H., Chen, Z.L., Han, S.Q., Li, Y., Yang, Y., Ye, B.Y., and Shi, W. (2014) SHRIMP U-Pb and Ar-Ar geochronology of major porphyry and skarn Cu deposits in the Balkhash Metallogenic Belt, Central Asia, and geological implications. Journal of Asian Earth Sciences, 79, 723-740.

Chi, G.X., Diamond, L.W., Lu, H.Z., Lai, J.Q., and Chu, H.X. (2021) Common problems and pitfalls in fluid inclusion study: A review and discussion. Minerals, 11, 7.

Choulet, F., Chen, Y., Wang, B., Faure, M., Cluzel, D., Charvet, J., Lin, W., and Xu, B. (2011) Late Paleozoic paleogeographic reconstruction of Western Central Asia based upon paleomagnetic data and its geodynamic implications. Journal of Asian Earth Sciences, 42, 867-884.

Cloos, M. (2001) Bubbling magma chambers, cupolas, and porphyry copper deposits. International Geology Review, 43, 285-311.

Cooke, D.R., Holling, P., and Walshe, J.L. (2005) Giant porphyry deposits: Characteristics, distribution, and tectonic controls. Economic Geology, 100, 801-818.

Crawford, M.L. (1981) Phase equilibria in aqueous fluid inclusions. In: Hollister, L.S. and Crawford, M.L. (eds). Fluid inclusions: Applications to petrology. Min Assoc Canada Short Course Handbook. 6, 75-100.

Elsenheimer, D., and Valley, J.W. (1993) Submillimeter scale zonation of $\delta^{18}O$ in quartz and feldspar, Isle of Skye, Scotland. Geochimica et Cosmochimica Acta, 57, 3669-3676.

Fall, A., and Bodnar, R.J. (2018) How Precisely Can the Temperature of a Fluid Event be Constrained Using Fluid Inclusions?. Economic Geology, 113, 1817-1843.

Fekete, S., Weis, P., Driesner, T., Bouvier, A.S., Baumgartner, L., and Heinrich, C.A. (2016) Contrasting hydrological processes of meteoric water incursion during magmatic-hydrothermal ore deposition: An oxygen isotope study by ion microprobe. Earth and Planetary Science Letter, 451, 263-271.

Fonseca Teixeira, L.M., Troch, J., and Bachmann, O. (2024) The dynamic nature of aTiO_2: Implications for Ti-based thermometers in magmatic systems. Geology, 52, 92-96.

Fournier, R.O. (1999) Hydrothermal Processes Related to Movement of Fluid From Plastic into Brittle Rock in the Magmatic-Epithermal Environment. Economic Geology, 94, 1193-1211.

Gao, S., Zou, X.Y., Hofstra, A.H., Qin, K.Z., Marsh, E.E., Bennett, M.M., Li, G.M., Jiang, J.L., Su, S.Q., Zhao, J.X., and Li, Z.Z. (2022) Trace elements in Quartz: Insights into source and fluid evolution in magmatic-hydrothermal systems. Economic Geology, 117, 1415-1428.

Ghiorso, M.S., and Gualda, G.A.R. (2013) A method for estimating the activity of titania in magmatic liquids from the compositions of coexisting rhombohedral and cubic iron–titanium oxides. Contributions to Mineralogy and Petrology, 165, 73-81.

Goldstein, R.H. (2001) Fluid inclusions in sedimentary and diagenetic systems. Lithos, 55, 159-193.

Gustafson, L.B., and Hunt, J.P. (1975) The porphyry copper deposit al El Salvador, Chile. Economic Geology, 70, 857-912.

Gustafson, L.B., and Quiroga, J. (1995) Patterns of mineralization and alteration below the porphyry copper orebody at El Salvador, Chile. Economic Geology, 90, 2-16.

Hayden, L.A., and Watson, E.B. (2007) Rutile saturation in hydrous siliceous melts and its bearing on Ti-thermometry of quartz and zircon. Earth and Planetary Science Letters, 258, 561-568.

Heinhorst, J., Lehmann, B., Ermolov, P., Serykh, V., and Zhurutin, S. (2000) Paleozoic crustal growth and metallogeny of Central Asia: evidence from magmatic-hydrothermal ore systems of Central Kazakhstan. Tectonophysics, 328, 69-87.

Hemley, J.J., Cygan, G.L., Fein, J.B., Robinson, G.R., and D’Angelo, W.M. (1992) Hydrothermal ore-forming processes in the light of studies in rockbuffered systems; I. Iron-copper-zinc-lead sulfide solubility relations. Economic Geology, 87, 1-22.

Henry, D.J., Guidotti, C.V., and Thomson, J.A. (2005) The Ti-saturation surface for low-to-medium pressure metapelitic biotites: Implications for geothermometry and Ti-substitution mechanisms. American Mineralogist, 90, 316-328.

Hou, Z., Yang, Z., Lu, Y., Kemp, A., Zheng, Y., Li, Q., Tang, J., Yang, Z., and Duan, L. (2015) A genetic linkage between subduction- and collision-related porphyry Cu deposits in continental collision zones. Geology, 43, 247-250.

Huang, K., Zhu, M.T., Zhang, L.C., Bai, Y., and Cai, Y.L. (2020) Geological and mineralogical constraints on the genesis of the Bilihe gold deposit in Inner Mongolia, China. Ore Geology Reviews, 124, 103607.

Huang, R.F., and Audétat, A. (2012) The titanium-in-quartz (TitaniQ) thermobarometer: a critical examination and re-calibration. Geochimica et Cosmochimica Acta, 84, 75-89.

Inoue, A., Inoue, S., and Utada, M. (2018) Application of chlorite thermometry to estimation of formation temperature and redox conditions. Clay Minerals, 53, 143-158.

Krylov, D.P., Zagnitko, V.N., Hoernes, S., Lugovaja, I.P., and Hoffbauer, R. (2002) Oxygen isotope fractionation between zircon and water: experimental determination and comparison with quartz-zircon calibrations. European Journal of Mineralogy, 14, 849-853.

Li, C.H., Shen, P., and Pan, H.D. (2018a) Mineralogy of the Aktogai giant porphyry Cu deposit in Kazakhstan: Insights into the fluid composition and oxygen fugacity evolution. Ore Geology Reviews, 95, 899-916.

Li, C.H., Shen, P., Pan, H.D., Cao, C., and Seitmuratova, E. (2018b) Geology and ore-forming fluid evolution of the Aktogai porphyry Cu deposit, Kazakhstan. Journal of Asian Earth Sciences, 165, 192-209.

Li, C.H., Shen, P., Pan, H.D., and Seitmuratova, E. (2019a) Control on the size of porphyry copper reserves in the North Balkhash–West Junggar Metallogenic Belt. Lithos, 328-329, 244-261.

Li, Y., Chen, X.H., Dong, S.W., Wang, Z.H., Chen, Z.L., Han, S.Q., Eleonora, S., Yang, Y., Ye, B.Y., Shi, W., and Chen, W. (2012) Metallogenic age of the super-large Aktogai porphyry copper deposit, Kazakhstan, and its exhumation history. Acta Geologica Sinica, 86, 295-306 (in Chinese with English abstract).

Li, Y., Li, X.H., Selby, D., and Li, J.W. (2018c) Pulsed magmatic fluid release for the formation of porphyry deposits: Tracing fluid evolution in absolute time from the Tibetan Qulong Cu‐Mo deposit. Geology, 46, 7-10.

Matsuhisa, Y. (1974) $^{18}O/^{16}O$ ratios for NBS-28 and some silicate reference samples. Geochemical Journal, 8, 103-107.

Matsuhisa, Y., Goldsmith, J.R., and Clayton, R.N. (1979) Oxygen isotopic fractionation in the system quartz-albite-anorthite-water. Geochimica et Cosmochimica Acta, 43, 1131-1140.

Mercer, C.N., Reed, M.H., and Mercer, C.M. (2015) Time scales of porphyry Cu deposit formation: Insights from titanium diffusion in quartz. Economic Geology, 110, 587-602.

Mining Data Solutions, Major Mines & Projects | Aktogay Mine. https://miningdataonline.com/property/4616/Aktogay-Mine.aspx#Reserves, 2022 (accessed 16 Aug 2022).

Monecke, T., Monecke, J., Reynolds, T.J., Tsuruoka, S., Bennett, M.M., Skewes, W.B., and Palin, R.M. (2018) Quartz Solubility in the H2O-NaCl System: A Framework for Understanding Vein Formation in Porphyry Copper Deposits. Economic Geology, 113, 1007-1046.

Monecke, T., Monecke, J., and Reynolds, T.J. (2019) The influence of CO_2 on the solubility of quartz in single-phase hydrothermal fluids: Implications for the formation of stockwork veins in porphyry copper deposits. Economic Geology, 114, 1195-1206.

Müller, A., Herrington, R., Armstrong, R., Seltmann, R., Kirwin, D.J., Stenina, N.G., and Kronz, A. (2010) Trace elements and cathodoluminescence of quartz in stockwork veins of Mongolian porphyry-style deposits. Mineralium Deposita, 45, 707-727.

Müller, A., Herklotz, G., and Giegling, H. (2018) Chemistry of quartz related to the Zinnwald/Cínovec Sn-W-Li greisen-type deposit, Eastern Erzgebirge, Germany. Journal of Geochemical Exploration, 190, 357-373.

Murakami, H., Seo, J.H., and Heinrich, C.A. (2010) The relation between Cu/Au ratio and formation depth of porphyry-style Cu–Au ± Mo deposits. Mineralium Deposita, 45, 11-21.

Mutch, E.J.F., Blundy, J.D., Tattitch, B.C., Cooper, F.J., and Brooker, R.A. (2016) An experimental study of amphibole stability in low-pressure granitic magmas and a revised Al-in-hornblende geobarometer. Contributions to Mineralogy and Petrology, 171, 85.

Pamukcu, A.S., Ghiorso, M.S., and Gualda, G.A.R. (2016) High-Ti, bright-CL rims in volcanic quartz: a result of very rapid growth. Contributions to Mineralogy and Petrology, 171, 105.

Park, J.W., Campbell, I.H., Chiaradia, M., Hao, H.D., and Lee, C.T. (2021) Crustal magmatic controls on the formation of porphyry copper deposits. Nature Reviews Earth & Environment, 2, 542-557.

Passchier, C., and Trouw, R. (2005) Microtectonics, p. 260. Springer Berlin.

Popov, V.S. (1996) Some problems of tectonics, magmatism, and metallogeny of Central Kazakhstan. In V. Shatov, R. Seltmann, A. Kremenetsky, B. Lehmann, V. Popov and P. Ermolov, Eds., Granite-related Ore Deposits of Central Kazakhstan and Adjacent Areas, p. 109-116. Glagol Publishing House.

Porter, T.M. (2016) The geology, structure and mineralisation of the Oyu Tolgoi porphyry copper-gold-molybdenum deposits, Mongolia: A review. Geoscience Frontiers, 7, 375-407.

Redmond, P.B., Einaudi, M.T., Inan, E.E., Landtwing, M.R., and Heinrich, C.A. (2004) Copper deposition by fluid cooling in intrusion-centered systems: New insights from the Bingham porphyry ore deposit, Utah. Geology, 32, 217-220.

Rempel, K.U., Williams-Jones, A.E., and Migdisov, A.A. (2008) The solubility of molybdenum dioxide and trioxide in HCl-bearing water vapour at 350°C and pressures up to 160 bars. Geochimica et Cosmochimica Acta, 72, 3074-3083.

Richards, J.P. (2011) Magmatic to hydrothermal metal fluxes in convergent and collided margins. Ore Geology Reviews, 40, 1-26.

Ridolf, F., and Renzulli, A. (2012) Calcic amphiboles in calc-alkaline and alkaline magmas: thermobarometric and chemometric empirical equations valid up to 1130 °C and 2.2 GPa. Contributions to Mineralogy and Petrology, 163, 877-895.

Roedder, E. (1984) Fluid inclusions. Geological Society of America Bulletin, 12, 644.

Rosso, K.M., and Bodnar, R.J. (1995) Microthermometric and Raman spectroscopic detection limits of CO2 in fluid inclusions and the Raman spectroscopic characterization of CO2. Geochimica et Cosmochimica Acta, 59, 3961-3975.

Rottier, B., and Casanova, V. (2021) Trace element composition of quartz from porphyry systems: a tracer of the mineralizing fluid evolution. Mineralium Deposita, 56, 843-862.

Rusk, B.G., Reed, M.H., and Dilles, J.H. (2008) Fluid inclusion evidence for magmatic-hydrothermal fluid evolution in the porphyry copper-molybdenum deposit at Butte, Montana. Economic Geology, 103, 307-334.

Rusk, B.G. (2012) Cathodoluminescent textures and trace elements in hydrothermal quartz. In J. Götze and R. Möckel, Eds., Quartz: deposits, mineralogy and analytics, p. 307-329. Springer Berlin.

Schirra, M., Laurent, O., Zwyer, T., Driesner, T., and Heinrich, C.A. (2022) Fluid Evolution at the Batu Hijau Porphyry Cu-Au Deposit, Indonesia: Hypogene Sulfde Precipitation from a Single-Phase Aqueous Magmatic Fluid During Chlorite–White-Mica Alteration. Economic Geology, 117, 979-1012.

Seedorff, E., Dilles, J.H., Proffett, J.M., Einaudi, M.T., Zurcher, L., Stavast, W.J.A., Johnson, D.A., and Barton, M.D. (2005) Porphyry deposits: Characteristics and origin of hypogene features. Economic Geology 100^{TH} Anniversary Volume, 251-298.

Seltmann, R., and Porter, T.M. (2005) The Porphyry Cu-Au/Mo Deposits of Central Eurasia: 1. Tectonic, Geologic & Metallogenic Setting and Significant Deposits. In T.M. Porter, Eds., Super Porphyry Copper and Gold Deposits: A Global Perspective, p. 467-512. PGC Publishing.

Seltmann, R., Porter, T.M., and Pirajno, F. (2014) Geodynamics and metallogeny of the central Eurasian porphyry and related epithermal mineral systems: A review. Journal of Asian Earth Sciences, 79, 810-841.

Shen, P., Pan, H.D., Xiao, W.J., Chen, X.H., Seitmuratova, E., and Shen, Y.C. (2013) Two geodynamic-metallogenic events in the Balkhash (Kazakhstan) and the West Junggar (China): Carboniferous porphyry Cu and Permian greisen W-Mo mineralization. International Geology Review, 55, 1660-1687.

Shen, P., Pan, H.D., Zhou, T.F., and Wang, J.B. (2014a) Petrography, geochemistry and geochronology of the host porphyries and associated alteration at the Tuwu Cu deposit, NW China: a case for increased depositional efficiency by reaction with mafic hostrock?. Mineralium Deposita, 49, 709-731.

Shen, P., Pan, H.D., and Dong, L.H. (2014b) Yandong porphyry Cu deposit, Xinjiang, China—Geology, geochemistry and SIMS U–Pb zircon geochronology of host porphyries and associated alteration and mineralization. Journal of Asian Earth Sciences, 80, 197-217.

Shen, P., Hattori, K., Pan, H.D., Jackson, S., and Seitmuratova, E. (2015) Oxidation Condition and Metal Fertility of Granitic Magmas: Zircon Trace-Element Data from Porphyry Cu Deposits in the Central Asian Orogenic Belt. Economic Geology, 110, 1861-1878.

Shen, P., Pan, H.D., Hattori, K., Cooke, D.R., and Seitmuratova, E. (2018) Large Paleozoic and Mesozoic porphyry deposits in the Central Asian Orogenic Belt: Geodynamic settings, magmatic sources, and genetic models. Gondwana Research, 58, 161-194.

Sillitoe, R.H. (2010) Porphyry copper systems. Economic Geology, 105, 3-41.

Steele-Macinnis, M., Lecumberri-Sanchez, P., and Bodnar, R.J. (2012) HokieFlincs_H_2O-NaCl: A microsoft excel spreadsheet for interpreting microthermometric data from fluid inclusions based on the PVTX, properties of H2O-NaCl. Computers & Geosciences, 49, 334-337.

Tang, G.Q., Li, X.H., Li, Q.L., Liu, Y., Ling, X.X., and Yin, Q.Z. (2015) Deciphering the physical mechanism of the topography effect for oxygen isotope measurements using a Cameca IMS-1280 SIMS. Journal of Analytical Atomic Spectrometry, 30, 950-956.

Tang, G.Q., Liu, Y., Li, Q.L., Feng, L.J., Wei, G.J., Su, W., Li, Y., Ren, G.H., and Li, X.H. (2020) New Natural and Fused Quartz Reference Materials for Oxygen Isotope

Microanalysis. Atomic Spectroscopy, 41, 188-193.

Terzer, S., Wassenaar, L.I., Araguás-Araguás, L.J., and Aggarwal, P.K. (2013) Global isoscapes for δ^{18}O and δ^{2}H in precipitation: improved prediction using regionalized climatic regression models. Hydrology and Earth System Sciences, 17, 4713-4728.

Thomas, J.B., Watson, E.B., Spear, F.S., Shemella, P.T., Nayak, S.K., and Lanzirotti, A. (2010) TitaniQ under pressure: the effect of pressure and temperature on the solubility of Ti in quartz. Contributions to Mineralogy and Petrology, 160, 743-759.

Tsuruoka, S., Monecke, T., and Reynolds, T.J. (2021) Evolution of the Magmatic-Hydrothermal System at the Santa Rita Porphyry Cu Deposit, New Mexico, USA: Importance of Intermediate-Density Fluids in Ore Formation. Economic Geology, 116, 1267-1284.

Uchida, E., Endo, S., and Makino, M. (2007) Relationship between solidification depth of granitic rocks and formation of hydrothermal ore deposits. Resource Geology, 57, 47-56.

Valley, J.W., and Graham, C.M. (1996) Ion microprobe analysis of oxygen isotope ratios in quartz from Skye granite: healed micro-cracks, fluid flow, and hydrothermal exchange. Contributions to Mineralogy and Petrology, 124, 225-234.

Van Den Kerkhof, A.M., and Hein, U.F. (2001) Fluid inclusion petrography. Lithos, 55, 27-47.

Wang, Y.F., Chen, H.Y., Baker, M.J., Han, J.S., Xiao, B., Yang, J.T., and Jourdan, F. (2019) Multiple mineralization events of the Paleozoic Tuwu porphyry copper deposit, Eastern Tianshan: evidence from geology, fluid inclusions, sulfur isotopes, and geochronology. Mineralium Deposita, 54, 1053-1076.

Wang, Y.H., Zhang, F.F., Xue, C.J., Liu, J.J., Zhang, Z.C., and Sun, M. (2021) Geology and Genesis of the Tuwu Porphyry Cu Deposit, Xinjiang, Northwest China. Economic Geology, 116, 471-500.

Weis, P., Driesner, T., and Heinrich, C.A. (2012) Porphyry-Copper Ore Shells Form at Stable Pressure-Temperature Fronts Within Dynamic Fluid Plumes. Science, 338, 1613-1616.

Wilke, S., Holtz, F., Neave, D.A., and Almeev, R. 2017. The effect of anorthite content and water on quartz-feldspar cotectic compositions in the rhyolitic system and implications for geobarometry. Journal of Petrology, 58, 789-818.

Windley, B.F., Alexeiev, D., Xiao, W.J., Kröner, A., and Badarch, G. (2007) Tectonic models for accretion of the Central Asian Orogenic Belt. Journal of the Geological Society, 164, 31-47.

Xiao, W.J., Kröner, A., and Windley, B. (2009) Geodynamic evolution of Central Asia in the Paleozoic and Mesozoic. International Journal of Earth Sciences, 98, 1185-1188.

Yakubchuk, A., Degtyarev, K., Maslennikov, V., Wurst, A., Stekhin, A., and Lobanov, K. (2012) Tectonomagmatic Settings, Architecture, and Metallogeny of the Central Asian Copper Province. Society of Economic Geologists, Inc. Special Publication, 16, 403-432.

Yang, Z.M., Goldfarb, R.J., and Chang, Z.S. (2016) Generation of postcollisional porphyry copper deposits in southern Tibet triggered by subduction of the Indian continental plate. In J.P. Richards, Eds., Tectonics and Metallogeny of the Tethyan Orogenic Belt, p. 279-300. Special Publications of the Society of Economic Geologists.

Zhang, C., Li, X., Almeev, R.R., Horn, I., Behrens, H., and Holtz, F. (2020) Ti-inquartz thermobarometry and TiO_2 solubility in rhyolitic melts: new experiments and parametrization. Earth and Planetary Science Letter, 538, 116-213.

Zhang, D.H., and Audétat, A. (2023) A Plea for More Skepticism Toward Fluid Inclusions: Part I. Postentrapment Changes in Fluid Density and Fluid Salinity Are Very Common. Economic Geology, 118, 15-41.

Zhong, R.C., Brugger, J., Chen, Y.J., and Li, W.B. (2015) Contrasting regimes of Cu, Zn and Pb transport in ore-forming hydrothermal fluids. Chemical Geology, 395, 154-164.

Zvezdov, V.S., Migachev, I.F., and Girfanov, M.M. (1993) Porphyry copper deposits of the CIS and the models of their formation. Ore Geology Reviews, 7, 511-549.

Figure captions

FIGURE 1. (**a**) The simplified map and main porphyry Cu±Au deposits of the CAOB (modified from Xiao et al. 2009; Shen et al. 2018). (**b**) The simplified geotectonic map of the Paleozoic of Kazakhstan and contiguous China (modified from Windley et al. 2007; Shen et al. 2013). Abbreviations: Cm = Cambrian; O = Ordovician; S = Silurian; D = Devonian; C = Carboniferous; P = Permian; PZ = Paleozoic; MZ = Mesozoic; CZ = Cenozoic; "1, 2, and 3" represent early, middle, and late, respectively.

FIGURE 2. (**a**) The geological map of the Aktogai Group (modified from Zvezdov et al. 1993; Seltmann et al. 2014). (**b**) The geological profile and (**c**) alteration and mineralization of the geological section in (**a**) (modified from Seltmann et al. 2014).

FIGURE 3. (**a**) A potassic altered rock. (**b**) Quartz-K-feldspar-dominated veins (A2 veins) crosscut discontinuous quartz stockworks and quartz veinlets (A1 veins). (**c**) Irregular K-feldspar-dominated veins (A2 veins) in the propylitic granodiorite with disseminated chalcopyrite and pyrite. (**d**) A quartz-chalcopyrite-molybdenite vein (B1 vein) crosscut quartz-chalcopyrite veins (B1 vein). (**e**) A quartz-chalcopyrite-chlorite vein (C vein) reopened a quartz-K-feldspar-chalcopyrite vein (B1 vein) along the edge. (**f**) A quartz-chalcopyrite-pyrite vein with thin K-feldspar halos (B2 vein). Abbreviations: Ccp = chalcopyrite; Kfs = K-feldspar; Py = pyrite.

FIGURE 4. The formation sequence of veins and quartz at Aktogai. Sketch maps are used to show the vein morphology, crosscut relationships, and mineral assemblages. A1 veins are shown with dashed lines because their walls are not easy to identify. The red and green lines represent quartz precipitation and dissolution, respectively, with the thickness of the lines indicating the abundance of quartz precipitation or dissolution. The figure also shows fluid inclusion types in different types of quartz. Abbreviation: Ab = albite; Anh = anhydrite; Bt = biotite; Ccp = chalcopyrite; Chl = chlorite; H = halite; Kfs = K-feldspar; Mol = molybdenite; Pl = plagioclase; Qz = quartz; Rt = rutile; Wm = white mica.

FIGURE 5. (**a**) CL images of a quartz phenocryst. Yellow arrows exhibit that the phenocryst rim showed brighter CL. (**b**) Ti and Al contents of the profile in (**a**). (**c**) Ti (ppm) vs. Al (ppm) diagram of the magmatic quartz.

FIGURE 6. (**a**) A quartz veinlet (A1 vein) crosscut by a quartz-K-feldspar vein (A2 vein). (**b**) CL images of the VQ_{A1} in quartz veinlet. (**c**) CL images of the VQ_{A2} in quartz-K-feldspar vein. (**d**) RQ_{bt} grains in an altered mafic mineral which was altered to hydrothermal biotite and magnetite. (**e**) RQ_{kfs} grains coexist with disseminated hydrothermal K-feldspar. The yellow dashed lines in (**b**) to (**e**) show the quartz underwent recrystallization and formed triple junctions. Abbreviations: Bt = biotite; Chl = chlorite;

Kfs = K-feldspar; Mt = magnetite; Qz = quartz; Wm = white mica.

FIGURE 7. (**a**) CL images of a quartz-K-feldspar-molybdenite-rutile vein (B1 vein). The edge of the vein (yellow dashed lines) underwent white mica alteration. Microfractures filled with VQ_{BC}, chalcopyrite, and chlorite. (**b**) VQ_{B1} grains underwent dissolution and were filled by VQ_{BC}. (**c**) VQ_{B1} grains with oscillatory growth zones. (**d**) A quartz-chalcopyrite-epidote-chlorite vein (C vein) crosscut a quartz-K-feldspar-chalcopyrite vein (B1 vein). The yellow dashed lines show the overgrowth of VQ_C along VQ_{B1}. The white dashed lines in (**a**), (**b**), and (**d**) show the full or partial recrystallization of VQ_{B1}. Abbreviation: Ccp = chalcopyrite; Flu = fluorite; Kfs = K-feldspar; Mol = molybdenite; Rt = rutile; Wm = white mica.

FIGURE 8. Variations of Ti and Al contents in typical profiles of (**a**) VQ_{B1} with oscillatory growth zones (Sample 09HS49-15-3), (**b**) VQ_{BC} precipitated between VQ_{B1} (Sample 09HS49-15-3), (**c**) VQ_C that crosscut VQ_{B1} (Sample 09HS49-12), and (**d**) VQ_{B2E} and VQ_{B2L} in B2 veins (Sample 09HS49-15-1). Profiles can be found in Fig. 7c, Fig. 7b, ESM Fig. 2a, and ESM Fig. 2b, respectively.

FIGURE 9. CL images of a quartz-chalcopyrite-pyrite vein (B2 vein). VQ_{B2L} grains contain incompletely dissolved VQ_{B2E} grains. Abbreviation: Ccp = chalcopyrite; Py = pyrite; Qz = quartz; Wm = white mica.

FIGURE 10. Box plots of (**a**) Ti (ppm), (**b**) Al (ppm), and (**c**) Al/Ti for hydrothermal quartz.

FIGURE 11. Distribution and characteristic features of fluid inclusions at Aktogai. (**a-b**) Distribution of FIAs in the growth zone of VQ_{A2} and microfractures. Boiling FIAs were found in the growth zone. (**c**) A boiling FIA in the VQ_{A2} rim. (**d**) FIAs in the growth zone crosscut by pseudosecondary and secondary FIAs in microfractures. (**e-f**) Boiling FIAs were found in the growth zone of VQ_{B1}. The early FIA occurs in CL-gray quartz, while the late one is in CL-black quartz. (**g**) A boiling FIA in the VQ_{B1} core. (**h**) An L-type FIA in the VQ_{BC}, which did not crosscut quartz boundaries. Abbreviation: Ap = apatite; Ccp = chalcopyrite; Chl = chlorite; Qz = quartz.

FIGURE 12. (**a**) Homogenization temperature $_{L\text{-}V}$ (°C) vs. homogenization temperature $_{halite}$ (°C) diagram for S-type fluid inclusions from different quartz types. The estimated pressures for S1-type fluid inclusions (after Lecumberri-Sanchez et al. 2012) are also shown. (**b**) Homogenization temperature (°C) vs. salinity (wt%) diagram for FIAs from different quartz types. Detailed data can be found in ESM Table 4. (**c-f**) Raman spectra of CO_2, anhydrite, rutile, and chalcopyrite in fluid inclusions from VQ_{B1}, VQ_{BC}, and VQ_C grains. Abbreviation: Anh = anhydrite; Ccp = chalcopyrite; H = halite; Hem = hematite; Qz = quartz; Rt = rutile.

FIGURE 13. Comparison of $T_{\text{Bt/Fluid inclusion}}$ (°C) and $T_{\text{Ti-in-quartz thermobarometry}}$ (°C). (**a**) $T_{\text{Bt/Fluid inclusion}}$ (°C) vs. $T_{\text{Thomas et al. (2010)}}$ (°C) diagram; (**b**) $T_{\text{Bt/Fluid inclusion}}$ (°C) vs. $T_{\text{Huang and Audétat (2012)}}$ (°C) diagram; (**c**) $T_{\text{Bt/Fluid inclusion}}$ (°C) vs. $T_{\text{Zhang et al. (2020)}}$ (°C) diagram. The average results of the biotite thermometer and the fluid inclusion corrected temperatures were used to plot. VQ_{B1} (1, 2, 3) and VQ_{BC} (1, 2) represent VQ_{B1} and VQ_{BC} in different veins.

FIGURE 14. $\delta^{18}O_{Qz}$ and $\delta^{18}O_{fluid}$ values (‰) of VQ_{B1} in different B1 veins. Abbreviation: Qz-Kfs-Mol vein = quartz-K-feldspar-molybdenite vein; Qz-Kfs-Ccp vein = quartz-K-feldspar-chalcopyrite vein.

FIGURE 15. The temperature (°C) vs. pressure (bar) diagram shows the fluid evolution at Aktogai (modified from Monecke et al. 2018). The relative abundance of selected hydrothermal minerals is also shown. Fluid evolution paths (i.e., arrows with different colors) are roughly constrained by the FIA types and the results of FIA and Ti-in-quartz thermobarometry.

Table 1 Summary of texture and trace element of quartz from different rocks and veins at Aktogai

Stages	Sample types	Quartz types	Mineral assemblages	Quartz characteristics	Data count	Ti (ppm) (average ± 1σ)	Al (ppm) (average ± 1σ)
Magmatic stage	Magmatic quartz	PQ_c	Qz, Ap, and Mt	Shape: Sub-round; Texture: Mottled; CL: gray	22	84 to 147 (123 ± 18)	106 to 929 (427 ± 219)
		PQ_r	Qz	Shape: Growing around MQZ-c as rims; Texture: Mottled; CL: bright	21	127 to 198 (165 ± 18)	164 to 993 (502 ± 187)
Potassic altered rock	Disseminated quartz	RQ_{bt}	Qz, Bt (partly altered to Chl), Fe-Ti oxides, and Rt	Shape: Sub-round or irregular; Texture: core-rim or complex; CL: gray, gray-black, and black	13	21 to 71 (49 ± 15)	55 to 359 (144 ± 92)
		RQ_{kfs}	Qz, Kfs, and	Shape: Aggregate or	24	27 to 98	64 to 573

			superposed Wm and Chl	irregular; Texture: Homogeneous or mottled; CL: gray		(45 ± 15)	(149 ± 126)
A1 veins	Qz veinlets	VQ_{A1}	Qz and superposed Wm	Shape: Sugar-granular or irregular; Texture: Homogeneous or mottled; CL: gray	30	40 to 212 (96 ± 36)	80 to 593 (174 ± 89)
A2 veins	Qz-Kfs veins	VQ_{A2} (gray CL)	Qz and Kfs and superposed Wm	Shape: Granular but growing vertically in the direction of walls; Texture: Wavy concentric and homogeneous or mottled; CL: gray and gray-black	16	42 to 100 (74 ± 12)	118 to 328 (161 ± 52)
		VQ_{A2} (gray-black CL)			5	34 to 54 (48 ± 8)	118 to 169 (143 ± 21)
B1 veins	Qz-Kfs-Mol-Rt veins	VQ_{B1}	Qz, Kfs, and Rt and superposed Wm	Shape: Large- to fine-grain; Texture: Growth zones and	12	13 to 39 (26 ± 8)	47 to 138 (94 ± 30)

				homogeneous; CL: gray and bright			
		VQ$_{BC}$	Qz and Mol	Shape: Irregular or veinlets, but growing close to the sulfide; Texture: Homogeneous; CL: black	n.d.	n.d.	n.d.
	Qz-Kfs-Mol veins	VQ$_{B1}$	Qz and Kfs and superposed Wm	Shape: Large- to fine-grain; Texture: Growth zones and homogeneous; CL: gray and bright	23	14 to 56 (27 ± 10)	39 to 229 (106 ± 50)
		VQ$_{BC}$	Qz and Mol	Shape: Irregular but growing close to the sulfide; Texture: Homogeneous; CL: black	6	11 to 22 (17 ± 4)	53 to 126 (76 ± 28)
	Qz-Kfs-Ccp veins	VQ$_{B1}$	Qz and Kfs and superposed Wm and	Shape: Large- to fine-grain; Texture: Homogeneous and	13	11 to 30 (21 ± 5)	47 to 284 (93 ± 61)

			clay	growth zones; CL: gray and bright			
		VQ_{BC}	Qz, Ccp, and Chl	Shape: Irregular but growing close to the sulfide; Texture: Homogeneous; CL: black	4	13 to 20 (17 ± 3)	69 to 116 (85 ± 21)
B2 veins	Qz-Ccp-Py veins	VQ_{B2E}	Qz and Kfs and superposed Wm	Shape: Large- to fine-grain; Texture: Growth zones and mottled; CL: gray and bright	11	36 to 75 (54 ± 13)	50 to 318 (93 ± 76)
		VQ_{B2L}	Qz, Ccp, and Py	Shape: Irregular veinlets or middle- to fine-grain, but growing close to the sulfide; Texture: Mottled and wavy concentric; CL: gray-black	12	14 to 63 (33 ± 13)	59 to 89 (71 ± 10)

C veins	Qz-Ccp-Chl veins	VQ_{BC}	Qz, Ccp, and Chl	Shape: Veinlets; Texture: Homogeneous; CL: black	6	10 to 23 (17 ± 5)	42 to 444 (134 ± 159)
	Qz-Ccp-Ep-Chl veins	VQ_{C}	Qz, Ccp, Flu, Ep, and Chl	Shape: Middle- to fine-grain, but growing towards the interior of veins; Texture: Homogeneous and growth zones; CL: black and black-gray	9	3 to 11 (8 ± 3)	11 to 381 (87 ± 113)

Note: The nomenclature of quartz types follows the sequence of quartz occurrence + stage ± generation. The first character "P", "V", and "R" represent "phenocrysts", "veins", and "altered rocks", respectively, and the second character "Q" stands for "quartz". The subscripted characters represent vein and alteration types, and the "E" and "L" in VQ_{B2E} and VQ_{B2L} stand for "early" and "late", respectively. Abbreviation: Ap = apatite; Bt = biotite; Ccp = chalcopyrite; Chl =chlorite; Ep = epidote; Flu = fluorite; Kfs = K-feldspar; Mt = magnetite; Mol = molybdenite; Py = pyrite; Rt = rutile; Qz = quartz; Wm = white mica. "n.d." represents no detection.

Table 2 Summary of fluid inclusion data from different rocks and veins at Aktogai

Qz type	Vein/rock type	FIA type	FIA count (FI count)	Size	Vapor volume (%)	$T_{m\text{-ice}}$ (°C)	$T_{h,\ \text{halite}}$ (°C)	T_h (°C)	Salinity (wt% NaCl)	P_h (bar)	Density (g/cm^3)
VQ_{A1}	A1 veins (discontinuous Qz veins)	L	7 (39)	4.3 to 11.4	40 to 60	-5.1 to -4.2	/	441 to 456	6.8 to 7.9	400 to 449	0.48 to 0.52
VQ_{A2}	A2 veins (Qz-Kfs veins)	V+S2	5 (32)	4.5 to 12.8	V: 70 to 90 S2: 20 to 30	V: -3.8 to -2.9	S2: 379 to 386	398 to 412	V: 4.7 to 6.1 S2: 45.0 to 45.9	V: 279 to 328 S2: 173 to 194	V: 0.51 to 0.56 S2: 1.05 to 1.06
		L	2 (10)	6.0 to 10.1	40 to 55	-4.8 to -4.3	/	422	6.9 to 7.6	335 to 336	0.55 to 0.56
		V	1 (3)	6.9 to 7.9	75 to 80	-2.9	/	390	4.8	253	0.58

$\mathrm{RQ}_{\mathrm{kfs}}$	Qz in disseminated potassic rocks	L	2 (13)	4.2 to 8.4	35 to 45	-4.0 to -3.9	/	390 to 413	6.3 to 6.5	249 to 312	0.56 to 0.61
		V	1 (3)	6.9 to 7.5	85	-4.1	/	410	6.6	304	0.57
$\mathrm{VQ}_{\mathrm{B1}}$	B1 veins (Qz-Kfs-Mol-Rt, Qz-Kfs-Mol, and Qz-Ccp-Kfs veins)	L	15 (61)	4.1 to 10.6	15 to 50	-3.8 to -1.2	/	345 to 390	2 to 6.1	152 to 253	0.55 to 0.65
		L+V	1 (4)	4.2 to 7.2	40 and 80	L: -1.7 V: -0.8	/	L: 378 V: 382	L: 2.8 V: 1.4	L: 224 V: 244	L: 0.57 V: 0.52
		V	1 (3)	6.2 to 7.5	70 to 80	-2.4	/	388	4.0	245	0.57
$\mathrm{VQ}_{\mathrm{B2E}}$	B2 veins (Qz-Ccp-Py veins with Kfs halos)	L	3 (11)	4.1 to 10.1	10 to 30	-2.4 to -1.9	/	303 to 328	3.2 to 4.0	88 to 123	0.70 to 0.75
$\mathrm{VQ}_{\mathrm{B2L}}$		L	3 (12)	4.1 to 11.5	10 to 30	-2.6 to -1.9	/	282 to 296	3.3 to 4.4	65 to 79	0.75 to 0.78
$\mathrm{VQ}_{\mathrm{BC}}$	B1 veins (Qz associated with Mol) and C veins	L	7 (26)	3.8 to 9.4	15 to 40	-2.4 to -1.0	/	322 to 341	1.7 to 4.0	114 to 145	0.66 to 0.68

	(Qz-Ccp-Chl veins)										
VQ_C	C veins (Qz-Ccp-Ep-Chl veins)	L	3 (9)	4.1 to 7.1	20 to 25	-2.1 to -1.5	/	264 to 279	2.6 to 3.5	49 to 62	0.78 to 0.80

Note: For $T_{m\text{-ice}}$, $T_{h,\ \text{halite}}$, T_h, salinity, P_h, and density, one FIA was used as one data. See ESM Table 4 for detailed data. “/” represents data unavailable. Abbreviation: Ccp = chalcopyrite; Chl = chlorite; Ep = epidote; FIA = fluid inclusion assemblages; Kfs = K-feldspar; Mol = molybdenite; Py = pyrite; Rt = rutile; Qz = quartz.

Table 3 Summary of values of oxygen isotope data (‰) of VQ_{B1} from different veins at Aktogai

Vein type	Quartz texture	$\delta^{18}O_{quartz}$ (‰)			Temperature (°C)	$\delta^{18}O_{fluid}$ (‰)			R
		Range (count)	Average	σ		Range	Average	σ	
Quartz-K-feldspar-molybdenite vein (B1 veins)	Oscillatory growth zones	8.94 to 9.55 (17)	9.21	0.17	380	4.42 to 5.04	4.70	0.17	89±1
Quartz-K-feldspar-chalcopyrite vein (B1 veins)	Oscillatory growth zones	8.65 to 9.07 (10)	8.84	0.11	371	3.91 to 4.33	4.10	0.11	86±1
	Homogeneous textures	8.81 to 9.13 (7)	8.96	0.11		4.06 to 4.30	4.22	0.11	86±1

Note: The fractionation equation of $\delta^{18}O_{quartz} - \delta^{18}O_{fluid} = 3.34 \times (10^6/(T + 273.15)^2) - 3.31$ (°C) provided by Matsuhisa et al. (1979) was used to estimate $\delta^{18}O_{fluid}$ values. The temperature used to estimate $\delta^{18}O_{fluid}$ values is the average corrected temperature obtained from fluid inclusion microthermometry. The percentage contribution of magmatic water in the fluid (R) was calculated by the equation of $\delta^{18}O_{fluid} = \delta^{18}O_{magmatic} \times R + \delta^{18}O_{meteoric} \times (1 - R)$. The $\delta^{18}O$ values for magmatic and meteoric water were assumed to be 6.31 ± 0.23 ‰ (Shen et al., 2018) and -8.90 ‰ (Terzer et al., 2013), respectively.

Figure 1

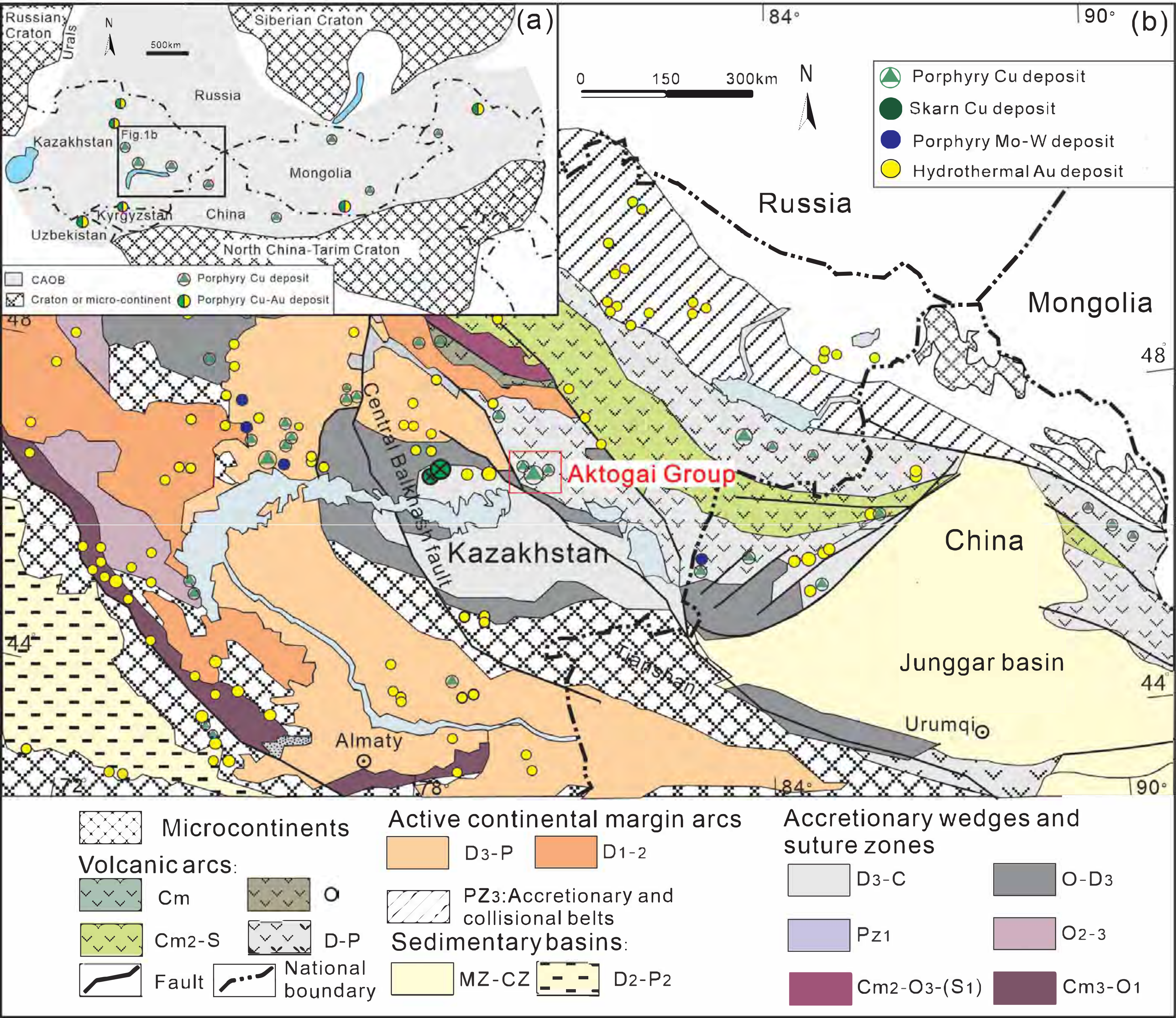
(a)
Russian Craton
Urals
N
500km
Siberian Craton
Russia
Kazakhstan
Fig.1b
Mongolia
Kyrgyzstan
China
Uzbekistan
North China-Tarim Craton
CAOB
Craton or micro-continent
Porphyry Cu deposit
Porphyry Cu-Au deposit
(b)
84°
90°
0
150
300km
N
Porphyry Cu deposit
Skarn Cu deposit
Porphyry Mo-W deposit
Hydrothermal Au deposit
Russia
Mongolia
48°
Central Balkhash fault
Aktogai Group
Kazakhstan
China
Junggar basin
Tianshan
Urumqi
Almaty
44°
72°
78°
84°
90°
Microcontinents
Volcanic arcs:
Cm
O
Cm_2-S
D-P
Fault
National boundary
Active continental margin arcs
D_3-P
D_{1-2}
PZ_3:Accretionary and collisional belts
Sedimentary basins:
MZ-CZ
D_2-P_2
Accretionary wedges and suture zones
D_3-C
O-D_3
Pz_1
O_{2-3}
Cm_2-O_3-(S_1)
Cm_3-O_1

Figure 2

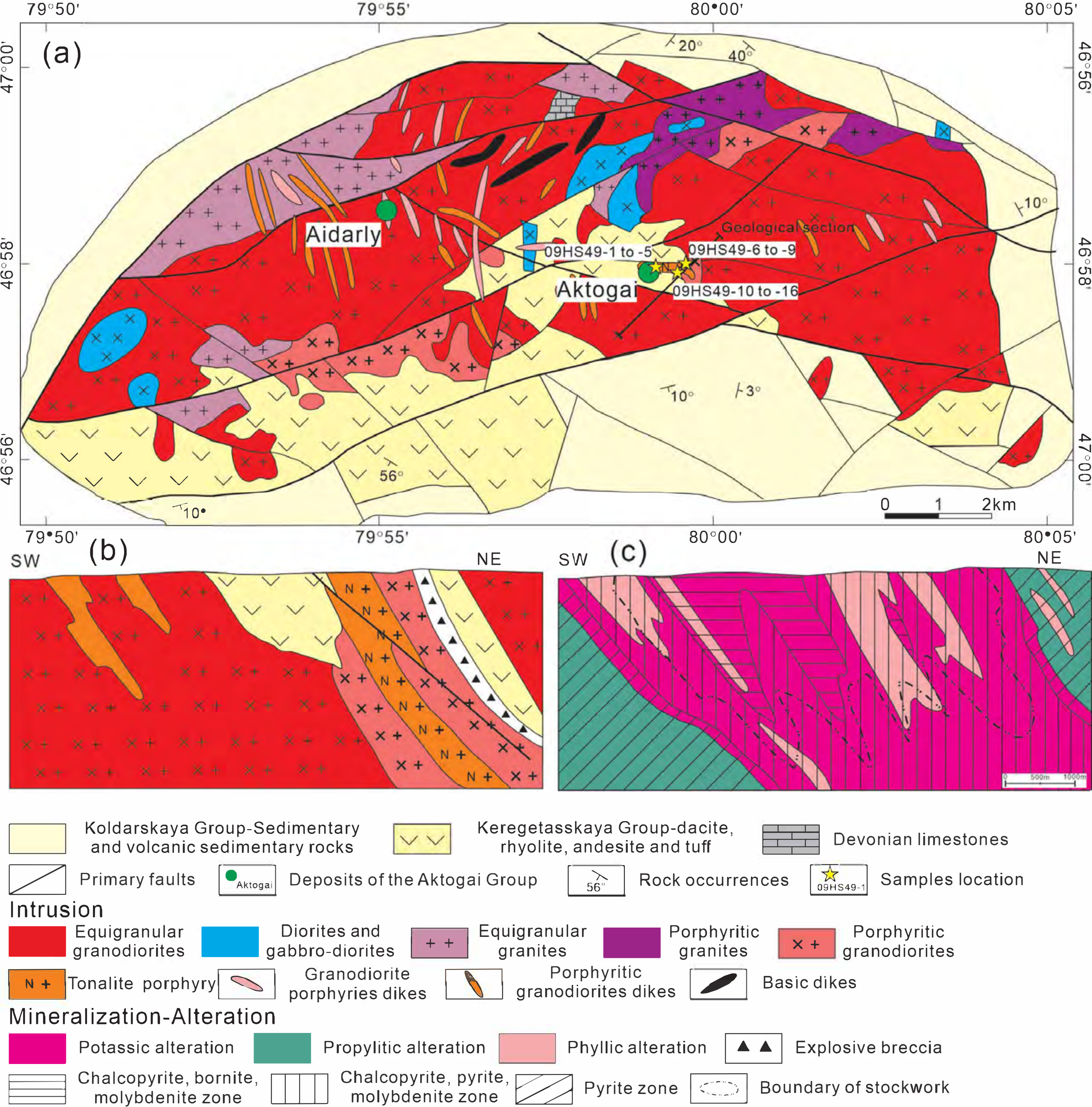

(a)
79°50'
79°55'
80°00'
80°05'
47°00'
46°58'
46°56'
20°
40°
10°
3°
56°
Aidarly
Aktogai
Geological section
09HS49-1 to -5
09HS49-6 to -9
09HS49-10 to -16
0
1
2km
(b)
SW
NE
(c)
SW
NE
0
500m
1000m
Koldarskaya Group-Sedimentary and volcanic sedimentary rocks
Keregetasskaya Group-dacite, rhyolite, andesite and tuff
Devonian limestones
Primary faults
Aktogai
Deposits of the Aktogai Group
56°
Rock occurrences
09HS49-1
Samples location
Intrusion
Equigranular granodiorites
Diorites and gabbro-diorites
Equigranular granites
Porphyritic granites
Porphyritic granodiorites
Tonalite porphyry
Granodiorite porphyries dikes
Porphyritic granodiorites dikes
Basic dikes
Mineralization-Alteration
Potassic alteration
Propylitic alteration
Phyllic alteration
Explosive breccia
Chalcopyrite, bornite, molybdenite zone
Chalcopyrite, pyrite, molybdenite zone
Pyrite zone
Boundary of stockwork

Figure 3

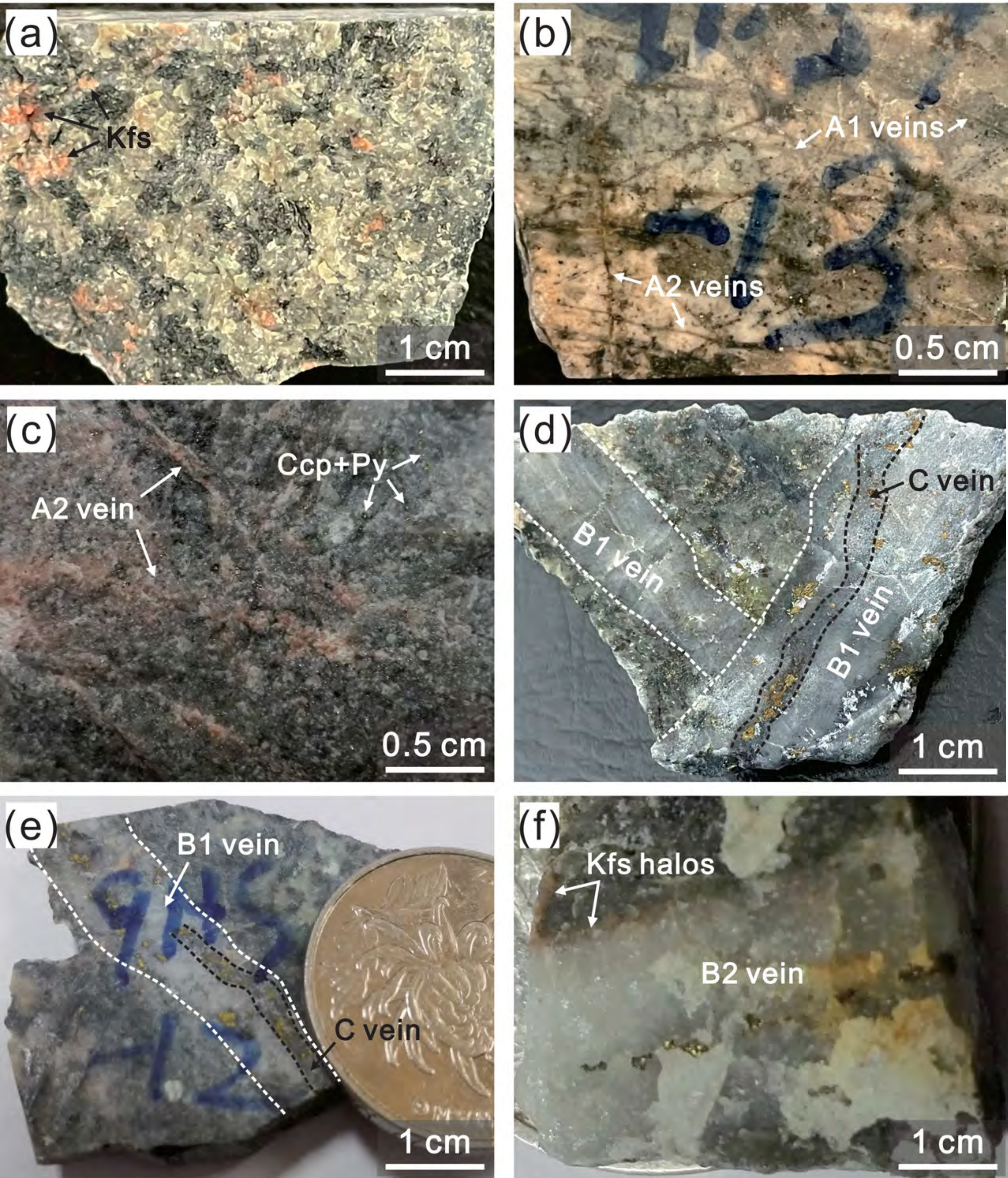

(a)
Kfs
1 cm
(b)
A1 veins
A2 veins
0.5 cm
(c)
A2 vein
Ccp+Py
0.5 cm
(d)
B1 vein
C vein
B1 vein
1 cm
(e)
B1 vein
C vein
1 cm
(f)
Kfs halos
B2 vein
1 cm

Figure 4

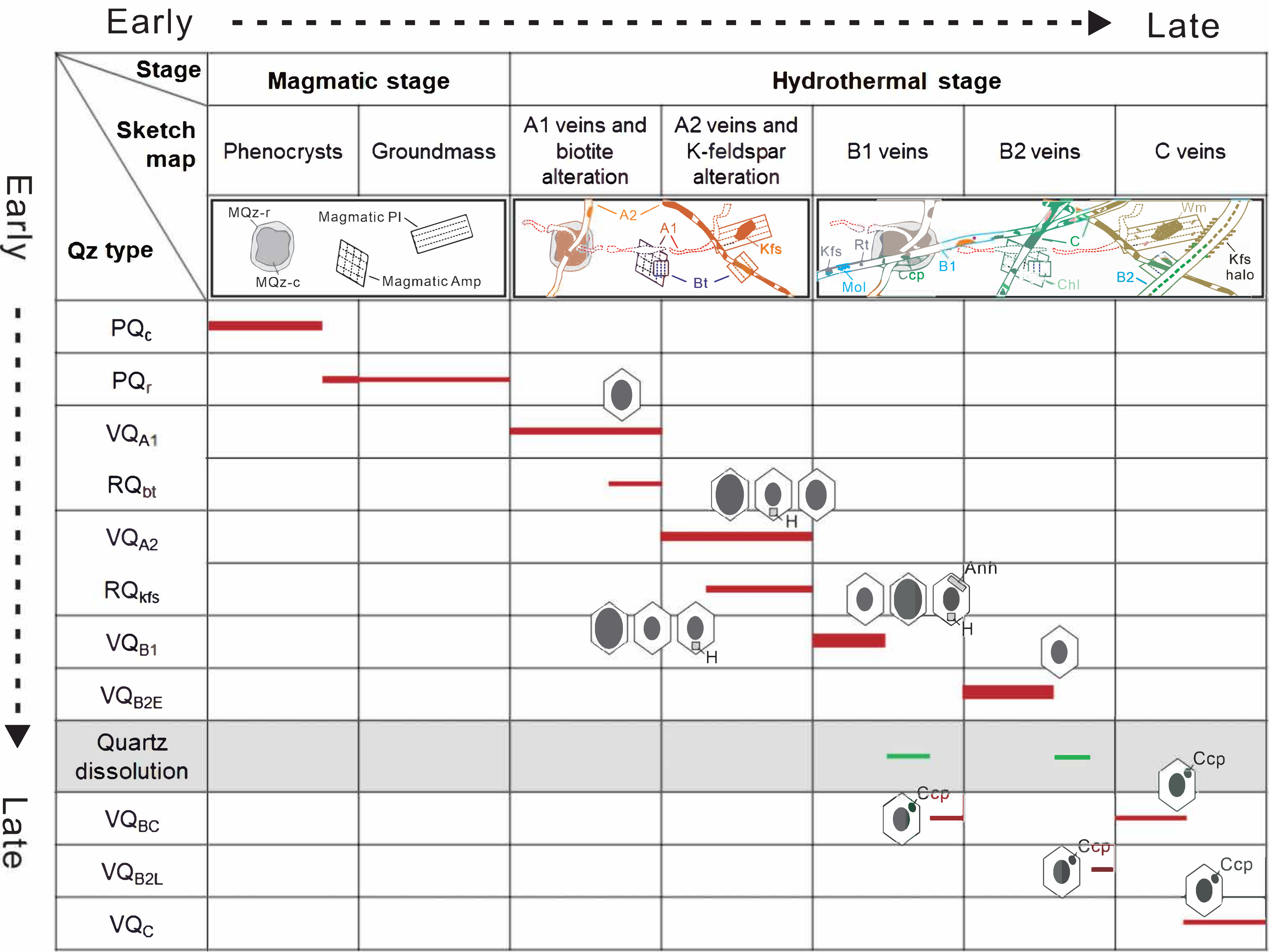
Early
Late
Stage
Sketch map
Qz type
Magmatic stage
Hydrothermal stage
Phenocrysts
Groundmass
A1 veins and biotite alteration
A2 veins and K-feldspar alteration
B1 veins
B2 veins
C veins
MQz-r
MQz-c
Magmatic Pl
Magmatic Amp
A2
A1
Kfs
Bt
Kfs
Rt
Mol
Ccp
B1
C
Chl
Wm
B2
Kfs halo
PQ_c
PQ_r
VQ_{A1}
RQ_{bt}
VQ_{A2}
RQ_{kfs}
VQ_{B1}
VQ_{B2E}
Quartz dissolution
VQ_{BC}
VQ_{B2L}
VQ_C
H
H
Anh
H
Ccp
Ccp
Ccp
Ccp
Early
Late

Figure 5


(a)
1
5
HFW: 559 µm
200 µm
2022-06-14
10:44:23
delmic
CL intensity
Dwell time: 12 µs
230 x
Emission: pass-through
(b)
Ti (ppm)
Al (ppm)
180
160
140
120
100
80
800
700
600
500
400
300
200
1
2
3
4
5
(c)
PQ$_c$
PQ$_r$
Ti (ppm)
200
180
160
140
120
100
80
0
200
400
600
800
1000
Al (ppm)

Figure 6

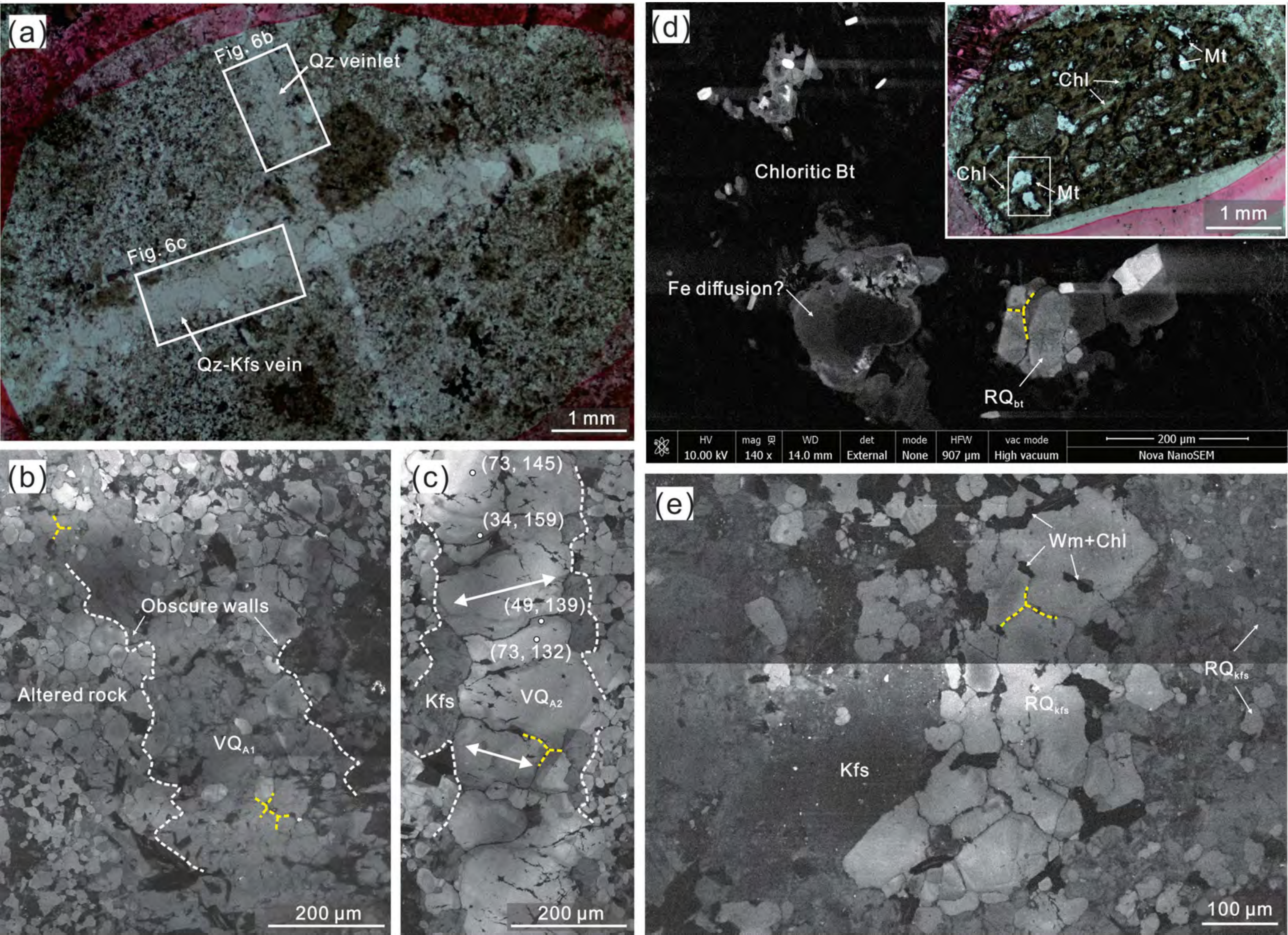
(a)
Fig. 6b
Qz veinlet
Fig. 6c
Qz-Kfs vein
1 mm
(b)
Obscure walls
Altered rock
VQ_{A1}
200 µm
(c)
(73, 145)
(34, 159)
(49, 139)
(73, 132)
Kfs
VQ_{A2}
200 µm
(d)
Chloritic Bt
Fe diffusion?
RQ_{bt}
Mt
Chl
Chl
Mt
1 mm
HV 10.00 kV
mag 140 x
WD 14.0 mm
det External
mode None
HFW 907 µm
vac mode High vacuum
200 µm
Nova NanoSEM
(e)
Wm+Chl
RQ_{kfs}
RQ_{kfs}
Kfs
100 µm

Figure 7

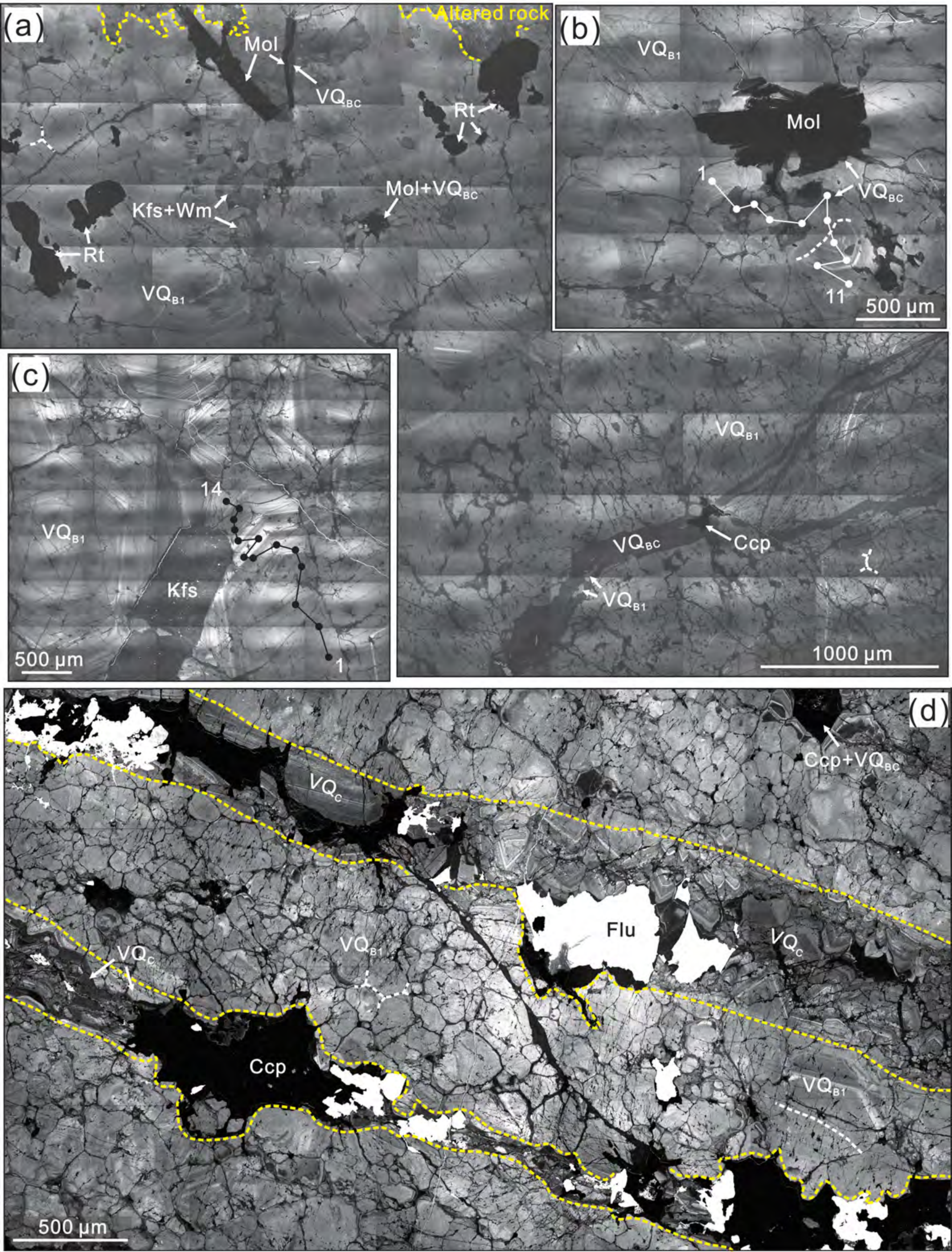
(a)
Altered rock
Mol
VQ$_{BC}$
Rt
Mol+VQ$_{BC}$
Kfs+Wm
Rt
VQ$_{B1}$
(b)
VQ$_{B1}$
Mol
1
VQ$_{BC}$
11
500 μm
(c)
14
VQ$_{B1}$
Kfs
500 μm
1
VQ$_{B1}$
VQ$_{BC}$
Ccp
VQ$_{B1}$
1000 μm
(d)
Ccp+VQ$_{BC}$
VQ$_{C}$
Flu
VQ$_{B1}$
VQ$_{C}$
VQ$_{C}$
Ccp
VQ$_{B1}$
500 μm

Figure 8

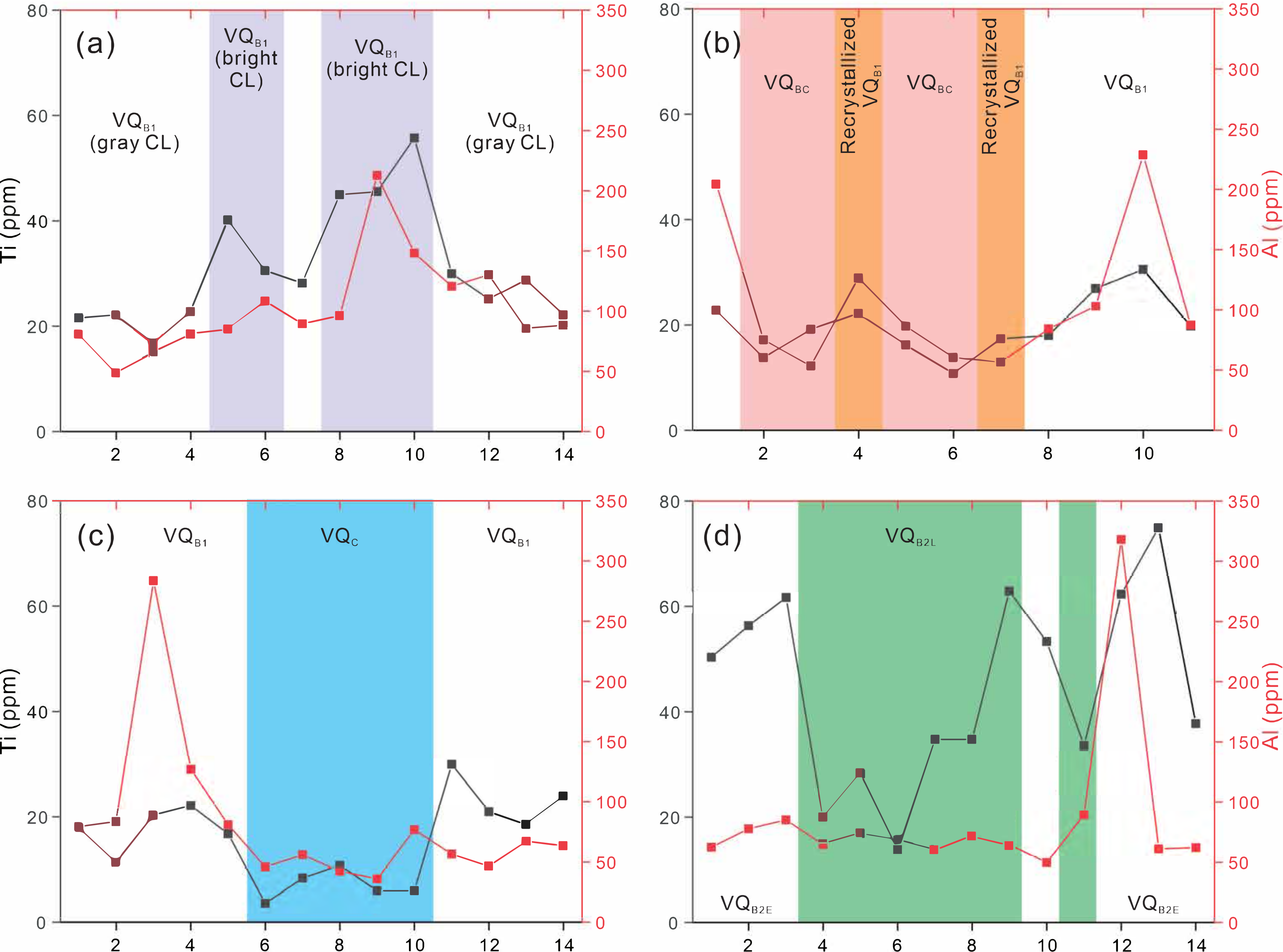

(a)
VQ$_{B1}$ (gray CL)
VQ$_{B1}$ (bright CL)
VQ$_{B1}$ (bright CL)
VQ$_{B1}$ (gray CL)
(b)
VQ$_{BC}$
Recrystallized VQ$_{B1}$
VQ$_{BC}$
Recrystallized VQ$_{B1}$
VQ$_{B1}$
(c)
VQ$_{B1}$
VQ$_{C}$
VQ$_{B1}$
(d)
VQ$_{B2L}$
VQ$_{B2E}$
VQ$_{B2E}$
Ti (ppm)
Al (ppm)
0
20
40
60
80
0
50
100
150
200
250
300
350
2
4
6
8
10
12
14

Figure 9

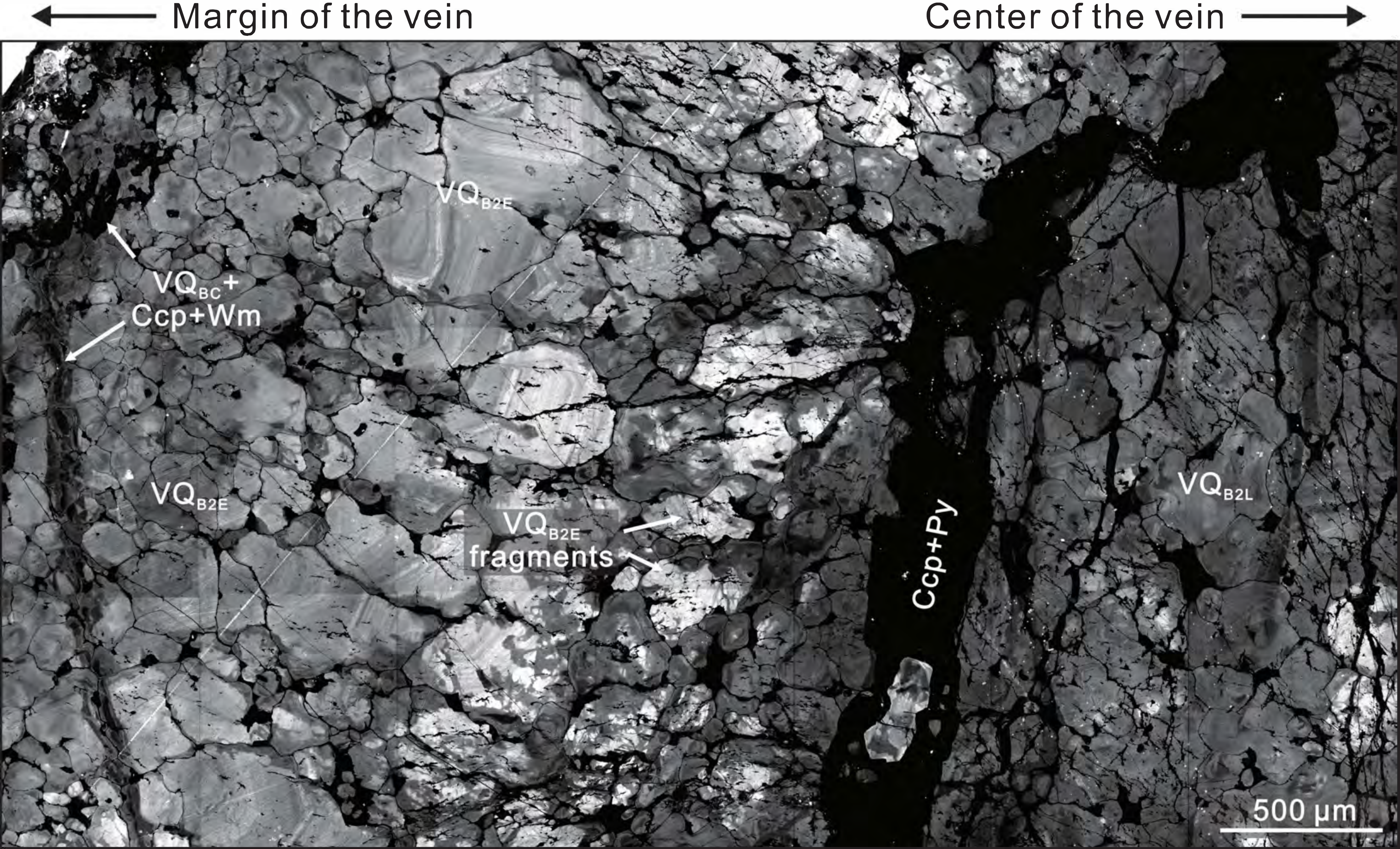

Margin of the vein
Center of the vein
VQ$_{B2E}$
VQ$_{BC}$+ Ccp+Wm
VQ$_{B2E}$
VQ$_{B2E}$ fragments
Ccp+Py
VQ$_{B2L}$
500 μm

Figure 10


(a)
Ti (ppm)
250
200
100
50
0
D.L. = 12 ppm
Outlier
75%+1.5IQR
75%
50%
25%
25%-1.5IQR
(b)
Al (ppm)
1000
100
10
D.L. = 11 ppm
(c)
Al/Ti
100
10
1
VQ$_{A1}$
RQ$_{bt}$
VQ$_{A2}$
RQ$_{kfs}$
VQ$_{B1}$
VQ$_{BC}$
VQ$_{C}$
VQ$_{B2}$

Figure 11

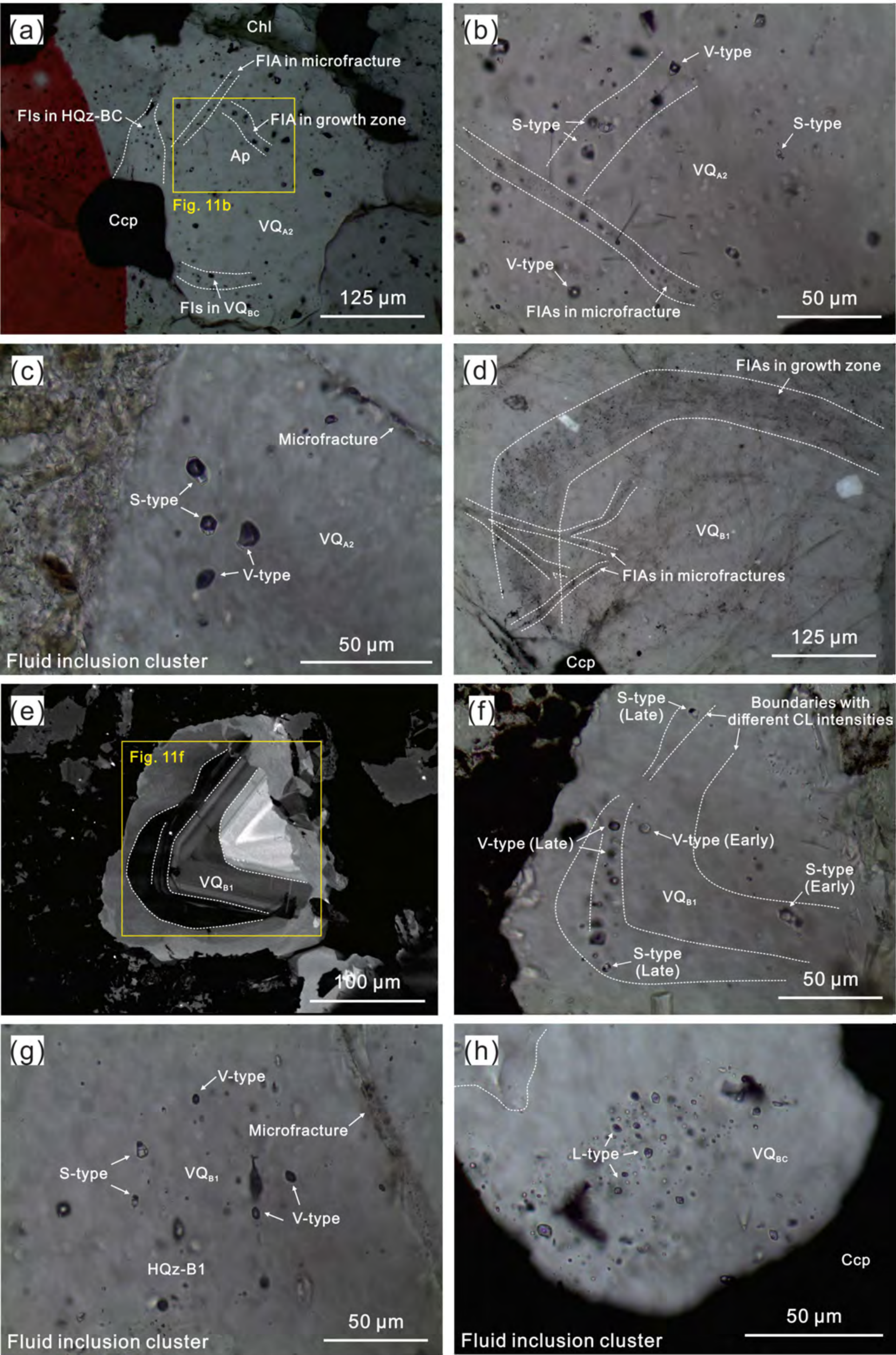
(a)
Chl
FIA in microfracture
FIs in HQz-BC
FIA in growth zone
Ap
Fig. 11b
Ccp
VQ_{A2}
FIs in VQ_{BC}
125 µm
(b)
V-type
S-type
S-type
VQ_{A2}
V-type
FIAs in microfracture
50 µm
(c)
Microfracture
S-type
VQ_{A2}
V-type
50 µm
Fluid inclusion cluster
(d)
FIAs in growth zone
VQ_{B1}
FIAs in microfractures
125 µm
Ccp
(e)
Fig. 11f
VQ_{B1}
100 µm
(f)
S-type (Late)
Boundaries with different CL intensities
V-type (Late)
V-type (Early)
S-type (Early)
VQ_{B1}
S-type (Late)
50 µm
(g)
V-type
Microfracture
S-type
VQ_{B1}
V-type
HQz-B1
50 µm
Fluid inclusion cluster
(h)
L-type
VQ_{BC}
Ccp
50 µm
Fluid inclusion cluster

Figure 12

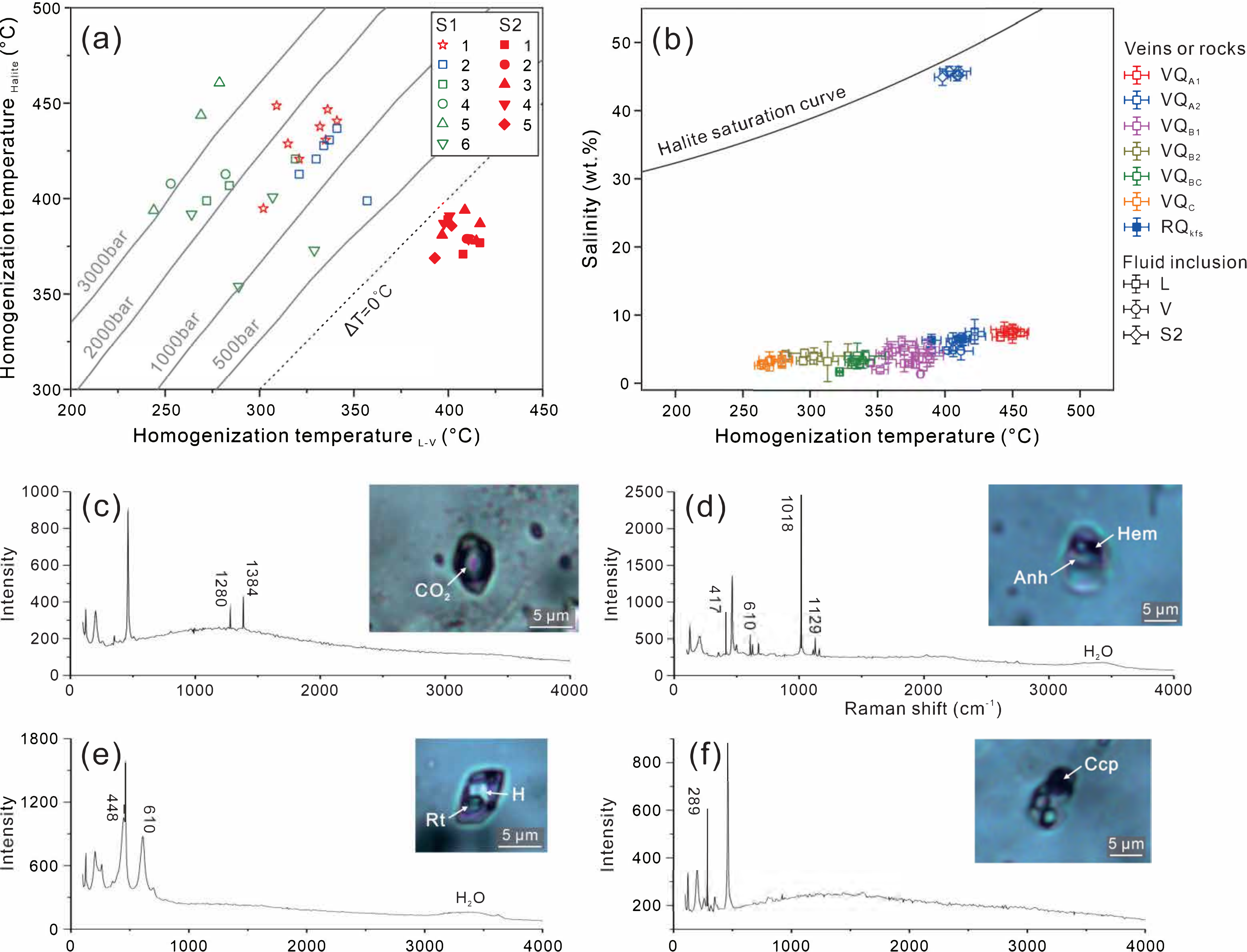
(a)
Homogenization temperature Halite (°C)
Homogenization temperature L-V (°C)
3000bar
2000bar
1000bar
500bar
ΔT=0°C
S1
S2
1
2
3
4
5
6
(b)
Salinity (wt.%)
Homogenization temperature (°C)
Halite saturation curve
Veins or rocks
VQA1
VQA2
VQB1
VQB2
VQBC
VQC
RQkfs
Fluid inclusion
L
V
S2
(c)
Intensity
1280
1384
CO2
5 μm
(d)
1018
417
610
1129
H2O
Hem
Anh
Raman shift (cm-1)
(e)
448
610
H
Rt
(f)
289
Ccp

Figure 13

(a)
(b)
(c)
T Thomas et al. (2010) (°C)
T Huang and Audétat (2012) (°C)
T Zhang et al. (2020) (°C)
T Bt/Fluid inclusion (°C)
ΔT = -100 °C
ΔT = -50 °C
ΔT = 0 °C
ΔT = +50 °C
250
300
350
400
450
500
550
600
650
700
VQ$_{A1}$
RQ$_{bt}$
VQ$_{A2}$
RQ$_{kfs}$
VQ$_{B1}$ (1)
VQ$_{BC}$ (1)
VQ$_{B1}$ (2)
VQ$_{BC}$ (2)
VQ$_{B1}$ (3)
VQ$_{C}$
VQ$_{B2E}$
VQ$_{B2L}$

Figure 14

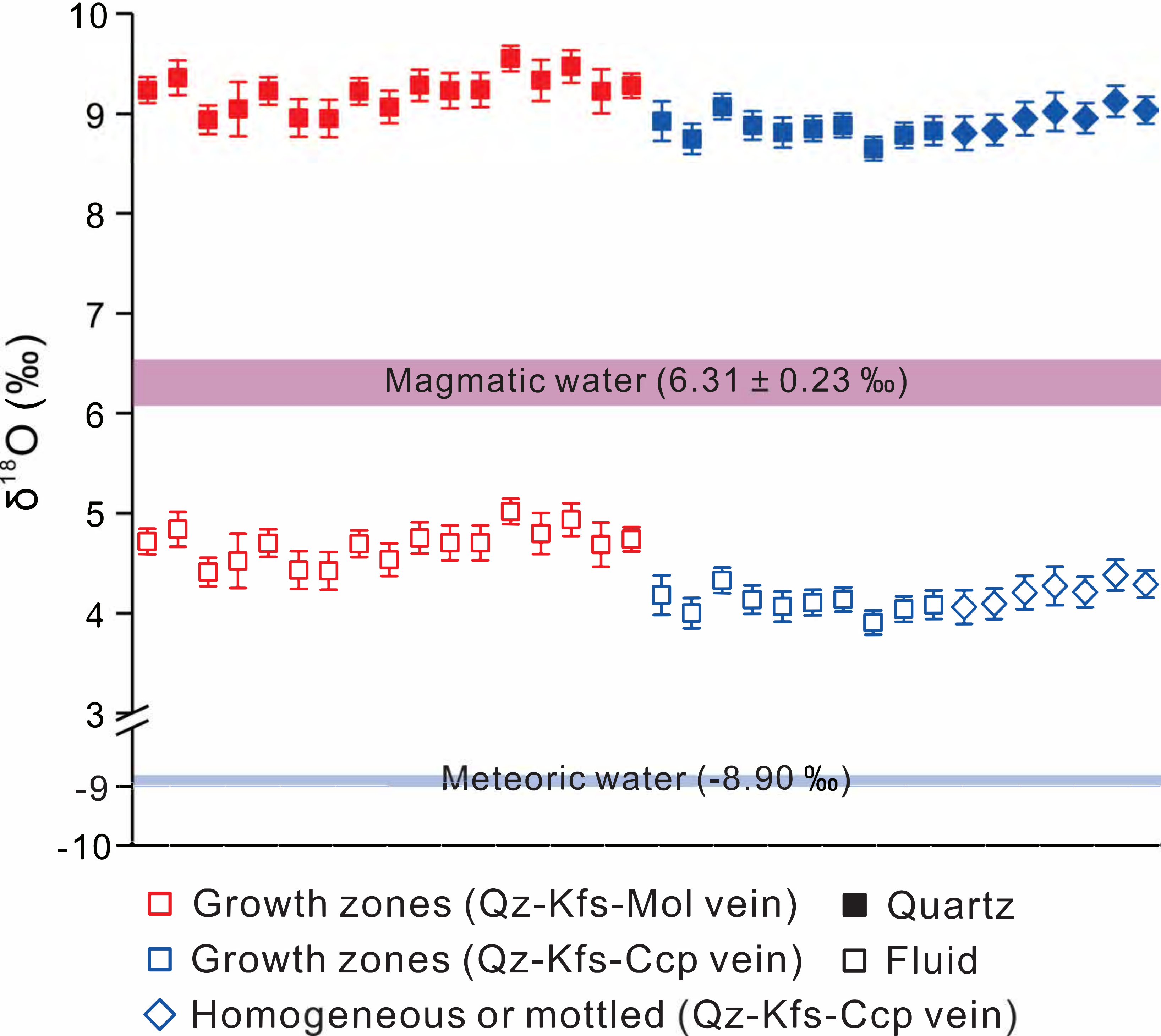
10
9
8
7
6
5
4
3
-9
-10
δ18O (‰)
Magmatic water (6.31 ± 0.23 ‰)
Meteoric water (-8.90 ‰)
Growth zones (Qz-Kfs-Mol vein)
Growth zones (Qz-Kfs-Ccp vein)
Homogeneous or mottled (Qz-Kfs-Ccp vein)
Quartz
Fluid

Figure 15

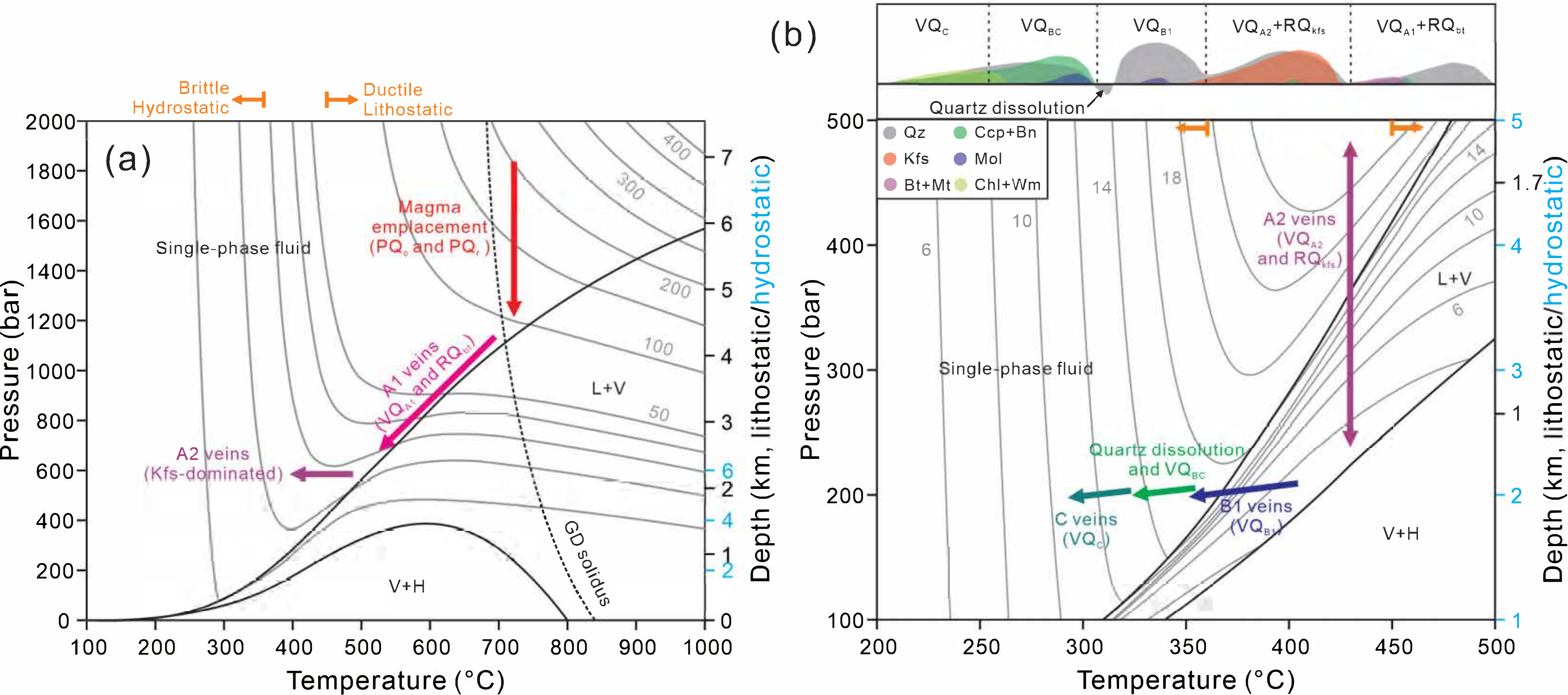
(a)
Brittle
Hydrostatic
Ductile
Lithostatic
Single-phase fluid
Magma emplacement (PQ_c and PQ_r)
A1 veins (VQ_{A1} and RQ_{bt})
A2 veins (Kfs-dominated)
L+V
V+H
GD solidus
400
300
200
100
50
Pressure (bar)
2000
1800
1600
1400
1200
1000
800
600
400
200
0
Temperature (°C)
100
200
300
400
500
600
700
800
900
1000
Depth (km, lithostatic/hydrostatic)
7
6
5
4
3
6
2
4
1
2
0
(b)
VQ_C
VQ_{BC}
VQ_{B1}
VQ_{A2}+RQ_{kfs}
VQ_{A1}+RQ_{bt}
Quartz dissolution
● Qz
● Ccp+Bn
● Kfs
● Mol
● Bt+Mt
● Chl+Wm
6
10
14
18
14
10
6
A2 veins (VQ_{A2} and RQ_{kfs})
L+V
Single-phase fluid
Quartz dissolution and VQ_{BC}
C veins (VQ_C)
B1 veins (VQ_{B1})
V+H
Pressure (bar)
500
400
300
200
100
Temperature (°C)
200
250
300
350
400
450
500
Depth (km, lithostatic/hydrostatic)
5
1.7
4
3
1
2
1